This is a post-peer-review, pre-copyedit version of an article published in *Space Science Reviews*. The final authenticated version is available online at: https://doi.org/10.1007/s11214-018-0537-y

A Pre-Landing Assessment of Regolith Properties at the InSight Landing Site

Paul Morgan[1], Matthias Grott[2], Brigitte Knapmeyer-Endrun[3], Matt Golombek[4], Pierre Delage[5], Philippe Lognonné[6], Sylvain Piqueux[4], Ingrid Daubar[4], Naomi Murdoch[7], Constantinos Charalambous[8], William T. Pike[8], Nils Müller[4], Axel Hagermann[9], Matt Siegler[10], Roy Lichtenheldt[11], Nick Teanby[12], Sharon Kedar[4]

Corresponding Author: Paul Morgan

Colorado School of Mines, 1801 19th St., Golden, CO 80401, USA

Email: morgan@mines.edu Tel: [+1] 303 384 2648

Affiliations:

[1] Colorado Geological Survey, Colorado School of Mines, 1801 19th St., Golden, CO 80401, USA

[2] DLR Institute for Planetary Research, Rutherfordstr. 2, 12489 Berlin, Germany

[3] Max Plank Institute for Solar System Research, Department Planets and Comets, Justus-von-Liebig-Weg 3, 37077 Göttinggen, Germany

[4] Jet Propulsion Laboratory, California Institute of Technology, 4800 Oak Grove Dr., Pasadena, CA 91109, USA

[5] Ecole des Ponts ParisTech, Laboratoire Navier (CERMES), Paris, France

[6] Institut de Physique du Globe de Paris –Sorbonne Paris Cité, Université Paris Diderot, 35 rue Hélène Brion, 75013 PARIS, France

[7] Institut Supérieur de l'Aéronautique et de l'Espace (ISAE-SUPAERO), Université de Toulouse, 31055 Toulouse Cedex 4, France

[8] Imperial College London, Faculty of Engineering, Department of Electrical and Electronic Engineering, London, UK

[9] The Open University, Faculty of Science Technology and Mathematics, Walton Hall, Milton Keynes MK7 6AA, UK

[10] Southern Methodist University, Deadman College of Humanities and Sciences, PO Box 750235, Dallas, TX 75275-0235, USA

[11] DLR Institute for System Dynamics and Control, Münchner Straße 20, 82234 Oberpfaffenhofen-Weßling, Germany

[12] University of Bristol, School of Earth Sciences, Wills Memorial Building, Queens Road, Clifton BS8 1RJ, UK

Acknowledgements

PM was supported for this work by subcontract no. 1479970 for the InSight Mission from the Jet Propulsion Laboratory. A portion of the work described in this paper was supported by the InSight Project at the Jet Propulsion Laboratory, California Institute of Technology, under a contract with the National Aeronautics and Space Administration. This is InSight Contribution Number 39.

Abstract

This article discusses relevant physical properties of the regolith at the Mars InSight landing site as understood prior to landing of the spacecraft. InSight will land in the northern lowland plains of Mars, close to the equator, where the regolith is estimated to be ≥ 3-5 m thick. These investigations of physical properties have relied on data collected from Mars orbital measurements, previously collected lander and rover data, results of studies of data and samples from Apollo lunar missions, laboratory measurements on regolith simulants, and theoretical studies. The investigations include changes in properties with depth and temperature. Mechanical properties investigated include density, grain-size distribution, cohesion, and angle of internal friction. Thermophysical properties include thermal inertia, surface emissivity and albedo, thermal conductivity and diffusivity, and specific heat. Regolith elastic properties not only include parameters that control seismic wave velocities in the immediate vicinity of the Insight lander but also coupling of the lander and other potential noise sources to the InSight broadband seismometer. The related properties include Poisson's ratio, P- and S-wave velocities, Young's modulus, and seismic attenuation. Finally, mass diffusivity was investigated to estimate gas movements in the regolith driven by atmospheric pressure changes. Physical properties presented here are all to some degree speculative. However, they form a basis for interpretation of the early data to be returned from the InSight mission.

Keywords

Mars, Regolith, Physical Properties, InSight Landing Site

57 Table of Contents

Introduction

The InSight mission is the first dedicated geophysical mission to another planet. InSight (Interior Exploration using Seismic Investigations, Geodesy and Heat Transport) will place a single geophysical lander on Mars to study its deep interior and to provide information relevant to the fundamental processes of terrestrial planet formation and evolution (Banerdt et al., 2013). This article discusses physical properties of the Mars regolith at the InSight landing site based upon information available approximately one year prior to launch, and eighteen months prior to touchdown of the InSight lander. The InSight mission represents many years of engineering and scientific design and preparation, based to some degree on the properties of the regolith at the landing site. Most of the scientific data to be collected by instruments on the InSight lander will be filtered by the regolith in the immediate vicinity of the landing site. Therefore to design these instruments and to make realistic predictions of the range of data characteristics that should be recorded by the instruments, a model of the physical properties of the landing site regolith has been required. As the science team approaches the final stages of preparation for first data return from the InSight Mission, we saw benefit in using a consistent set of regolith physical property values for any required data processing and early publications across the project. At least some of these property values will be revised at a later date with new data from the InSight instruments.

The InSight lander is based on a lander used for the successful Phoenix mission that was launched to Mars on August 4, 2007 and investigated near-surface ice in the Martian Arctic (Smith et al., 2009). Scientific instruments on the Phoenix lander have been replaced by a broad-band seismometer that will be placed on the surface of Mars, a heat-flow probe with an internal hammer mechanism that will hammer itself into the Martian regolith with an accompanying radiometer to determine the radiative surface temperature of the regolith close to the lander, and a precision tracking system. Additional instruments on the lander will measure orbital and local atmospheric parameters of Mars. Some regolith properties, such as radioactivity and magnetic properties have been omitted in this discussion because they were either not pertinent to the InSight Mission instruments or they lacked data at the regolith scale.

The InSight landing site is shown on a portion of Mars topography in Figure 1. The general landing area was chosen for basic operational reasons of being close to the equator for year-round solar power for the lander and smooth topography for the landing site. More specific details of landing site selection are given in the Landing Site Overview in section 2.1 below. Mars has two basic terrains, smooth northern lowland plains (“planitia”) and southern cratered highlands (“terra”), separated by the dichotomy

boundary. Four geologic eras have been assigned to terrains on Mars based on crater densities: Pre-Noachian, 4.5 – 4.1 Ga; Noachian, 4.1 – 3.7 Ga; Hesperian, 3.7 – 3.0 Ga; and Amazonian, 3.0 Ga – present. The landing site is in lowlands terrain of Early Hesperian or younger age, just north of the dichotomy boundary.

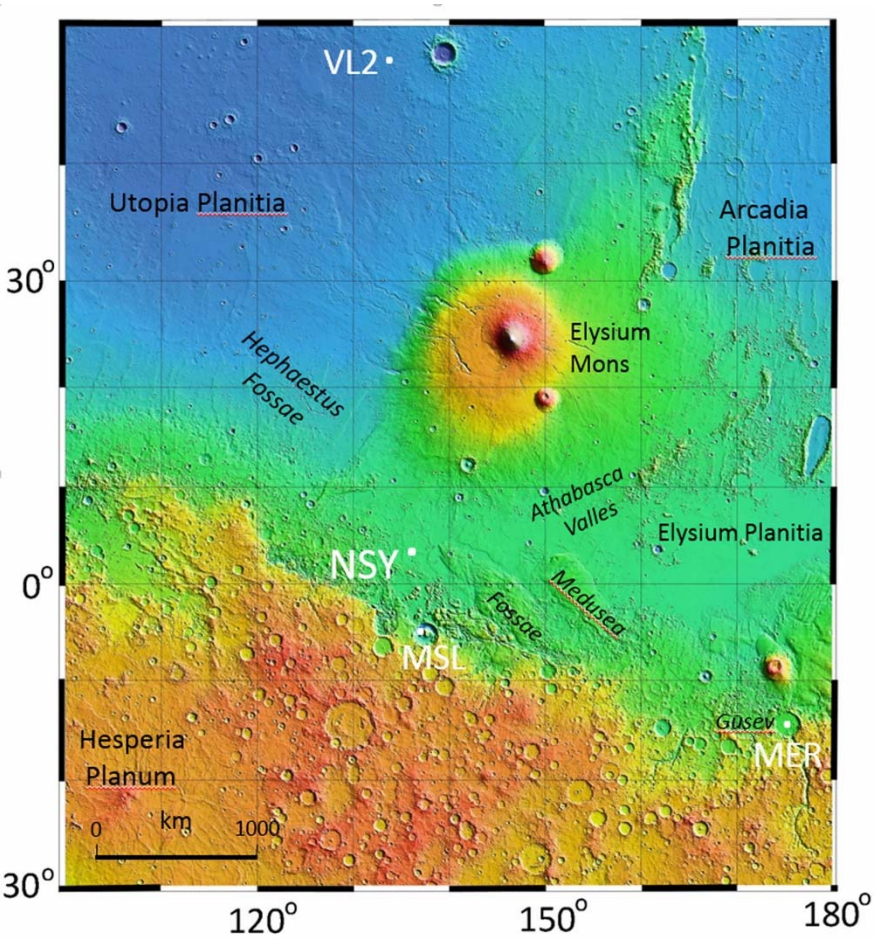

Figure 1: Topographic map of the region around the InSight landing site (NSY) showing major physiographic features, mentioned in the text, as well as the Viking Lander 2 (VL2), Mars Science Laboratory (MSL), and Mars Exploration Rover (MER) Spirit landing sites. Spirit landed in Gusev crater and Curiosity (MSL) landed in Gale crater. The map is a portion of the Mars Orbiter Laser Altimeter (MOLA) topographic map of Mars (Smith et al., 2001).

Following this introduction is a description of the regolith at the landing site including the criteria and process of landing site selection. This section is followed by four regolith physical property sections: Regolith Soil Mechanical Properties; Regolith Thermo-Physical Properties; Regolith Elastic Properties; and Mass Diffusivity. The paper closes with a summary and conclusions section. Sections were contributed by different authors or groups of authors according to their specialty. We have endeavored to make the

document flow as smoothly as possible, but it is primarily an informational article. However, what the paper lacks in style we hope that it contributes in utility.

1. Regolith at the InSight Landing Site

This section describes properties of the regolith essential for safe landing and operation of the spacecraft and instrument deployment.

1.1. Landing Site Overview

InSight will land in western Elysium Planitia on Hesperian plains just north of the dichotomy boundary (Golombek et al., 2017). This location satisfies the three dominant landing site engineering constraints, which are latitude (3°N-5°N), elevation (<-2.5 km with respect to the MOLA geoid), and a large smooth, flat surface to place a 130 km by 27 km landing ellipse. Other engineering constraints that are relevant to the geologic setting include: 1) a load bearing, radar reflective surface with thermal inertia >100–140 J/(m^2 K $s^{1/2}$), slopes <15° and rock abundance <10% for safe landing and instrument deployment, and a broken up regolith >3 m thick to facilitate deployment of the heat flow probe (Golombek et al., 2017).

The InSight landing ellipse is located on smooth plains with Noachian highlands to the south and west, a ridge of Medusae Fossae Formation to the southeast and very young lavas from Athabasca Valles to the east (Golombek et al., 2017). The ellipse is located at 4.5°N, 135.9°E, about 540 km north of the Mars Science Laboratory landing site. The plains surface on which the InSight ellipse is located is mapped as Early Hesperian transition unit (eHt) by Tanaka et al. (2014) in the global geologic map of Mars, which could be sedimentary or volcanic. A volcanic interpretation of the plains is supported by: 1) the presence of rocks in the ejecta of fresh craters ~0.4 to 20 km diameter suggesting a strong competent layer ~4 to 200 m deep with weaker material above and below (e.g., Golombek et al., 2013; Catling et al., 2011, 2012; Warner et al., 2017); 2) exposures of strong, jointed bedrock overlain by ~10 m of relatively fine grained regolith in nearby Hephaestus Fossae in southern Utopia Planitia at 21.9°N, 122.0°E (Golombek et al., 2013, 2017); 3) platy and smooth Late Hesperian to Early Amazonian lava flows up to 200 m thick mapped in 6 m/pixel visible images south of the landing site (Ansan et al., 2015); and 4) the presence of wrinkle ridges, which have been interpreted to be fault-propagation folds, in which slip on thrust faults at depth is accommodated by asymmetric folding in strong, but weakly bonded layered material (such as basalt flows) near the surface (e.g., Mueller and Golombek, 2004; Golombek and Phillips, 2010).

The landing ellipse has very low rock abundance (Golombek et al., 2017). Most rocks at the landing site are concentrated around rocky ejecta craters larger than 30 to 200 m diameter, but not around similarly fresh smaller craters (Golombek et al., 2013, 2017). Because ejecta is sourced from shallow depths, ~0.08 times the diameter of the crater (Melosh, 1989), and based on the assumption that the surface morphology is fresh and not highly eroded, the onset diameter of rocky ejecta craters has been used to map the thickness of the broken up regolith. Results indicate a regolith that is 3-17 m thick (Warner et al., 2014, 2016, 2017), that grades into large blocky ejecta over strong intact basalts (Golombek et al., 2013, 2017). Because fresh craters larger than 2 km do not have rocky ejecta, material below the basalts at ~200 m depth is likely weakly bonded sediments.

Surficial thermophysical properties of the landing site indicate that the soil that makes up the surface materials is similar to common weakly bonded soils on Earth and conducive to penetration by the heat flow probe (Golombek et al., 2017). The thermal inertia of the landing ellipse is about 200 J/(m^2 K $s^{1/2}$), the albedo is 0.25, and dust cover index is 0.94 (see Section 4.2, and Golombek et al., 2017). Comparison with the thermal inertias of previous landing sites and the soils at these sites (Golombek et al., 2008a) suggests the InSight landing site surfaces are composed of cohesionless sand or low cohesion soils (cohesions of less than a few kPa, angle of internal friction of 30-40°), with bulk densities of ~1000 to 1600 kg/m^3, particle sizes of ~150-250 μm (fine sand), that extend to a depth of at least several tens of centimeters, and with surficial dust layer less than 1–2 mm thick (Golombek et al., 2017).

The albedo and dust cover index are similar to dusty and low-rock abundance portions of the Gusev cratered plains, which are Hesperian lava flows with an impact generated regolith, modified by eolian processes (Golombek et al., 2006). Mapping of surface terrains in high-resolution images of the InSight landing site and surrounding areas, shows these terrains are similarly Hesperian lava flows with an impact generated regolith modified by eolian processes (Golombek et al., 2017; Warner et al., 2017).

An exposed escarpment of nearby Hephaestus Fossae (Figure 2) shows this near surface structure with ~10 m thick, relatively fine grained regolith, that grades into coarse, blocky ejecta with meter to ten-meter scale boulders that overlies strong, jointed bedrock. The grading of finer grained regolith into coarser, blocky ejecta is exactly what would be expected for a surface impacted by craters with a steeply dipping negative power-law size distribution in which smaller impacts vastly outnumber larger impacts that would excavate more deeply beneath the surface (e.g., Shoemaker and Morris, 1969; Hartmann et al., 2001; Wilcox et al., 2005).

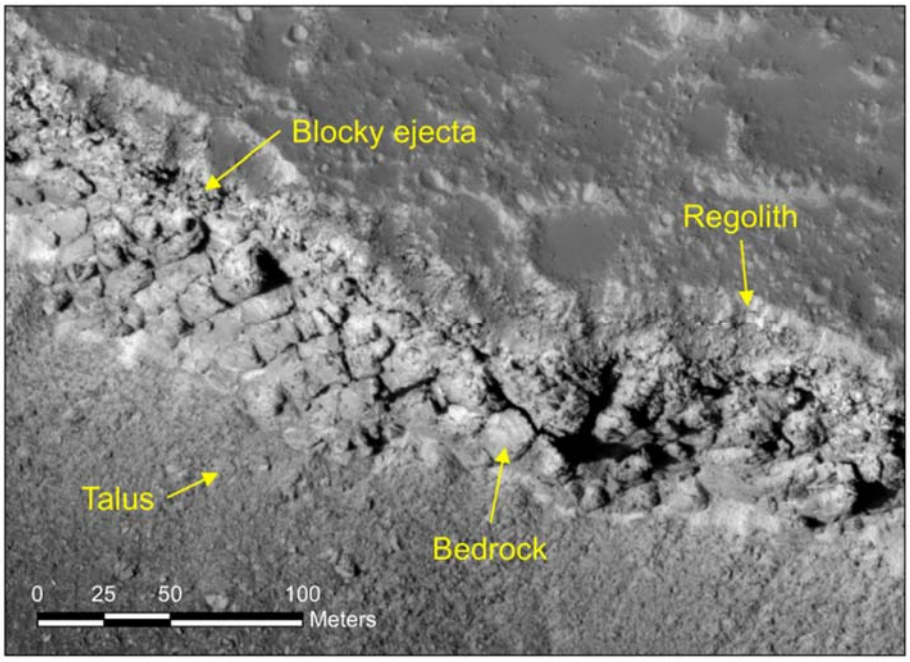

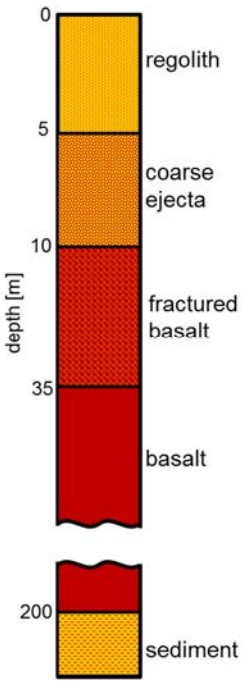

Figure 2: Left: An example of the shallow structure of the InSight landing site. HiRISE image PSP_002359_2020 of a portion of the exposed steep scarp of the Hephaestus Fossae in southern Utopia Planitia at 21.9°N, 122.0°E showing ~10 m thick, fine grained regolith, that grades into coarse, blocky ejecta that overlies strong, jointed bedrock (arrows show each). Right: Stratigraphic model of the shallow subsurface in the InSight landing region based on geological interpretation of orbital data and analysis of rocky crater ejecta. Figure modified from Knapmeyer-Endrun et al., 2016.

1.2. Rock Abundance

The contrast between measurements of thermal emission from the surface at various wavelengths using the Viking Orbiter Infrared Thermal Mapper (IRTM) and the Mars Global Surveyor spacecraft Thermal Emission Spectrometer (TES) data have been used to determine the rock abundance (the fractional area covered by high thermal inertia rocky material) at about 60 and 8 km/pixel scales (Christensen, 1986; Nowicki and Christensen, 2007). With the rock abundance and the bulk thermal inertia, the thermal inertia of the remaining soil, referred to as the fine-component thermal inertia (Kieffer et al., 1977), has also been determined (Christensen, 1986; Nowicki and Christensen, 2007). Rock abundance estimated from thermal differencing is 4% and 9% for IRTM pixels of ~60 km (Christensen, 1986) and around 4% (1%–7%) for TES pixels of ~8 km (Nowicki and Christensen, 2007) in the landing ellipse. Because the thermal differencing estimates of rock abundance are relatively low for this area

(Christensen, 1986; Nowicki and Christensen, 2007), the fine component thermal inertia is only slightly lower than the bulk thermal inertia.

Rock abundance measured from shadows in HiRISE images fit to model exponential cumulative fractional area versus diameter curves in 150 m bins (Golombek et al., 2008b, 2012) also indicate a very low average rock abundance of 1-2% for the InSight landing site (Golombek et al., 2017), although rock abundance can increase to ~35% around rocky ejecta craters. Fragmentation theory in which the particle size distribution is described by a negative binomial function (Charalambous, 2014) was applied to the InSight landing site using cratering size-frequency measurements to derive a synthesized regolith with a size-frequency distribution similar to the exponential model for ~2-6% rock abundance (Charalambous et al., 2011; Golombek et al., 2017). The measurements and models of rock abundance combined with the thermal inertia observations all indicate a relatively fine-grained regolith with low rock abundance in the upper 5 m of the regolith at the landing site.

1.3.Regolith Structure Summary

In summary, the upper 5 m of regolith at the landing site are expected to be dominantly composed of nearly cohesionless fine basaltic sand, which contains few rocks. The regolith was produced by impact gardening of basalt flows with eolian sorting and transport of the sand. In contrast with lunar regolith, the sand grains are rounded to sub-rounded by saltation (e.g., McGlynn et al., 2011). With increasing depth, larger particles and rocks are expected to become more plentiful until the upper, relatively fine-grained regolith grades into a coarse-grained breccia or blocky ejecta that overlies fractured basalt flows. In addition, with increasing depth the effects of impact decreases and basalt would likely be less fractured. Below ~200 m basalt would transition to sediments or weakly bonded sedimentary rocks.

2. Regolith Soil Mechanical Properties

2.1 Introduction

The parameters used to characterize the mechanical properties of the regolith at the InSight landing site are considered in this section. They are also summarized in a table in the Appendix.

The Martian regolith is expected to be a complex mix of weathered, indurated, and windblown material (e.g., Putzig and Mellon, 2007), and apart from engineering safety considerations, the InSight landing site was chosen to facilitate penetration of the HP^3 thermal probe to a depth of 3-5 m into a column of fragmented regolith (Golombek et al., 2017). Comparison with data from other landed missions and orbiters indicates that the regolith is largely cohesionless, has angle of internal friction close to that of sand (30-40°), and particles are expected to be rounded due to erosion by wind. Indeed, eolian activity on Mars has occurred throughout geologic time. The surface layer has been subjected to eolian activity and impacts: after each impact sand size grains have been saltated and rounded and sorted and the entire column of material has rounded (sub-rounded) grains. As such, the region may be viewed as an eolian deposit which may be the result of potentially several inflation and deflation periods. Given the values of thermal inertia (200 J/(m^2 K^1 s$^{1/2}$)), albedo (0.25) and dust cover index (0.94) in the InSight landing place, and based on comparison with the thermal inertias of previous landing sites, the InSight surfaces are composed of cohesionless sand or low cohesion soils with particle sizes of ~0.15-0.25 mm (fine sand) (Golombek et al., 2008a, 2017).

2.2 Density

Physical properties of regoliths, such as thermal conductivity, seismic velocity, penetration resistance, shear strength, compressibility and dielectric constant, depend on bulk density, which depends on grain size distribution, grain shape, particle surface texture and grain arrangement (Carrier et al., 1973). In dust powders, repulsive effects of electrostatic forces can result in densities as low as 1000 kg/m^3; in fine sand, inter-particle forces are mainly governed by gravity and inter-granular friction, resulting in higher densities. However, it is likely that the lower gravity on Mars could result in looser arrangements of grains of same shape and size distribution, compared to the gravity on the earth. Possible values of the regolith density can be further estimated by considering typical features of granular assemblies and sands, together with the physical properties of some terrestrial sands and regolith simulants (Mojave simulant, Eifelsand, and Mars Soil Simulant-D; Delage et al., 2017). A simple illustration providing first order estimates can be obtained from geometrical considerations of arrangements of spherical particles of the same diameter. In the densest possible arrangement (tetrahedral), with a minimum void ratio e_{min} = 0.351, with terrestrial sands, often composed of quartz grains with a density of 2670 kg/m^3, this value corresponds to a maximum bulk density of 1980 kg/m^3, a high density for (non-basaltic) terrestrial sands. For basaltic sands, as on Mars and in some areas on the earth, the corresponding density would be 2230 kg/m^3 with a grain density of 3310 kg/m^3 for basalt. Conversely, the loosest possible assembly of spheres

(simple cubic) has a maximum void ratio e_{max} = 0.908, yielding a minimum bulk density of 1400 kg/m^3 for quartz sands and of 1580 kg/m^3 for basaltic sands. For non-spherical grain shapes, other configurations are possible. For example, elongated grains, with aspect ratios significantly different from one, may exhibit rotational interlocking, particles resting against each other building bridges that increase void space. Limited overburden pressure can prevent particles from rotating and form statically stable regimes, supported in the low gravity of Mars, and especially prevalent in particle packages that have not be subject to strong external loading. Once loaded or subject to vibration, these packages will tend to increase in density.

On the Moon, regolith density drastically increases at depths below 20 cm. This increase has been attributed to the effects of continuing small meteoroid impacts, not filtered by an atmosphere as on Mars. Small impacts generate a loose, stirred-up surface while at the same time densifying the underlying soil (Carrier et al., 1973). Details of this process are not fully understood (Heiken et al., 1991), but best estimates for typical average densities are 1450 to 1550/kg m^3 at depths between 0 and 15 cm and 1690 to 1790 kg/m^3 at depths between 30 and 60 cm. In addition, analyses of the heat flow experiment data emplaced at the Apollo 15 and 17 sites indicates that the bulk density must be approximately 1300 kg/m^3 at the surface and must rise steeply in the upper few centimeters in order to be consistent with nighttime surface temperature data (Keihm et al., 1973; Keihm and Langseth, 1973, 1975; Langseth et al., 1976). The situation is, however, quite different on Mars because micometeorites are stopped by the atmosphere. The primary shallow processes are wind transport and saltation of sand-size particles.

In natural sands, a non-uniform grain size distribution provides denser arrangements, with smaller grains filling voids between larger grains. Irregular angular grains allow for looser packing than spherical grains. This is expected to be the case for the InSight landing site, with surface densities estimated to be around 1300 kg m^{-3} (see below). Bolton (1986) provided the minimum (e_{min}) and maximum (e_{max}) void ratios and densities of a series of terrestrial sands. The loosest sands were two river sands (Welland River, Canada, and Chattahoochee River, USA) with bulk densities of 1390 and 1290 kg/m^3, respectively. Note that river sands are known to be rounded due to transportation in water. Sand on Mars is rounded during saltation (McGlynn et al., 2011). Both the minimum (1290 kg/m^3) and maximum (1910 kg/m^3) densities provided by Bolton (1986) are not too far from densities obtained from simple geometrical considerations on the ideal granular arrangements of spheres. In addition, observations made by previous landers and rovers also showed bulk densities in the range of 1100–1300 kg/m^3 and 1150 ± 150 kg/m^3 for surficial sand and sandy soil deposits (see, e.g., Golombek et al., 2008a; Herkenhoff et al., 2008, and references

293 therein). Based on the fact that surface thermal inertia values are most compatible with a sand to crusty-
294 cloddy soil deposits (Golombek et al., 2008a) and given the above considerations on terrestrial sands, the
295 current best estimate for the regolith surface density is close to 1300 kg/m^3. In addition, a friction angle
296 of about 30° would also correspond to this density range (Delage et al., 2017).

297 In general, density is expected to increase with depth as a function of overburden pressure following
298 an exponential relation (e.g., Robinson and Gluyas, 1992; Revil et al., 2002), but compressibility of Mars
299 analogue material was found to be small, with an increase in density of around 20 kg/m^3 from the surface
300 to 5 m depth (Delage et al., 2017), such that this effect can generally be neglected for the depth range
301 relevant here. Regolith particles on Mars initially originate from the comminution caused by impacts on
302 the surface, prior to being affected by eolian transportation and saltation that result in reducing their
303 initial angularity to produce rounded or sub-rounded sorted grains. While repeated excavation, breakup,
304 and movement by wind would result in a rather loose packing of grains, subsequent vibrational
305 compaction due to, e.g., seismic events may compact the soil to significant depth, as is observed on the
306 Moon (Carrier et al., 1973, 1974; Heiken et al., 1991). In addition, saltation of grains during the soil
307 deposition can be a high energy process and compact the soil, and relative densities in excess of 90% have
308 been observed in accretional deposits on terrestrial sand dunes (Denekamp and Tsur-Lavie, 1981).
309 Therefore, a model of regolith density for the InSight landing site should allow for some compaction to be
310 present.

311 Regolith structure may locally deviate from the model proposed above in regions where craters have
312 been filled with fine grained material due to eolian activity. This has been observed, for example, in the
313 Gusev plains, where craters with diameters between 20 and 100 m are abundant in all stages of erosion
314 (Golombek et al., 2006). Given a depth to diameter ratio of typically 0.2 for simple craters, filling by fine
315 grained material could provide lens of dominantly sand-sized material in the subsurface that have not
316 been mixed with rocks or other material by subsequent impacts.

317 To describe the lunar density data, a hyperbolic density relationship was established which reasonably
318 reproduces densities to a depth of 3 m. However, that this description is based on no physical model.
319 Rather, it was chosen because linearly, superlinearly, or exponentially increasing profiles yield unrealistic
320 values at the surface or at larger depths (Heiken et al., 1991), although they also fit the available data. In
321 its general form, density may then be written as:

$$\rho(z) = \rho_{inf}\frac{A+z}{B+z} \quad (1)$$

where $\rho(z)$ is density ρ as a function of depth, ρ_{inf} is the density at depth and z is the depth below the Martian surface in meters. A and B are constants with the dimensions of length that describe

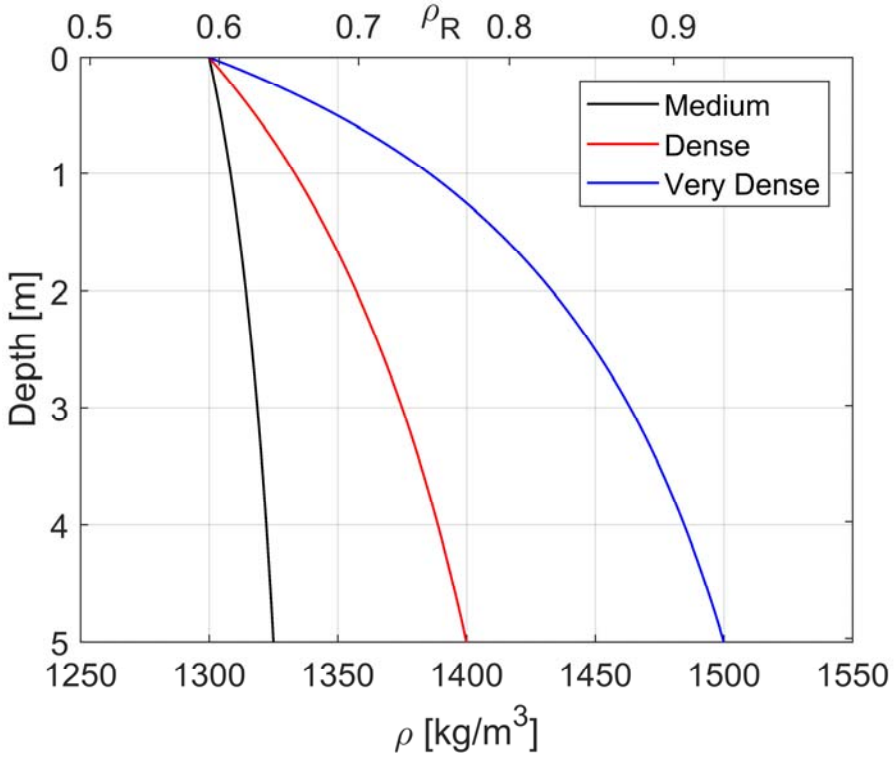

Figure 3: Model density as a function of depth for the upper five meters of regolith at the InSight landing site. The three profiles correspond to different states of regolith compaction. Upper axis gives relative density assuming a specific density of 2800 kg/m^3 minimum as well as maximum void ratios of 0.75 and 1.5, respectively, close to the values measured for the MMS-Sand Mars analogue material (Vrettos et al., 2014).

the chosen density profile, and example coefficients corresponding to the cases shown in Figure

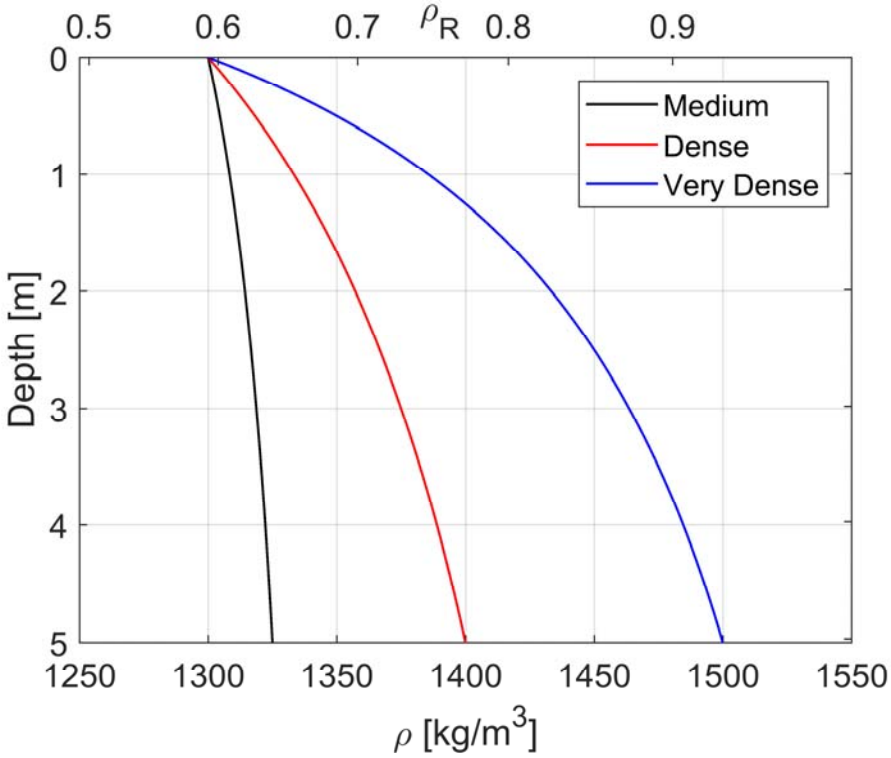

Figure 3 are given in Table 1. As a reference, a surface density of 1300 kg/m^3 seems to be most compatible with the available constraints, and three different compaction models are shown. If void ratios between e_{min} = 0.75 and e_{max} = 1.5 are assumed in accordance with measurements on Mars regolith analogue material (Vrettos et al., 2014), relative densities between 0.6 (moderately compacted) and >0.9 (densely compacted) are obtained at 5 m depth.

Table 1: Parameters used to calculate density profiles for the different cases shown in Figure 3.

Case	ρ_{max} (kg/m^3)	A (m)	B (m)
Medium Compacted	1350	4.81	5
Densely Compacted	1500	4.33	5
Very Densely Compacted	1600	2.03	2.5

2.3 Cohesion

Cohesion, a component of the shear strength, of surface materials on Mars has been determined from soil mechanics experiments performed by arms and scoops on fixed landers and by the interaction of wheels of rovers with surface materials by rovers. The two Viking landers and the Phoenix lander had arms that trenched surface materials while monitoring motor currents to yield force, and imaging systems to observe the deformed materials (Moore et al., 1977, 1987; Shaw et al., 2009). The Mars Pathfinder rover, Sojourner, the two Mars Exploration Rovers, Spirit and Opportunity, and the Mars Science Laboratory rover, Curiosity, performed wheel trenching and terramechanics experiments, while monitoring motor currents to derive wheel torques, and imaged the deformed materials (Moore et al., 1999; Herkenhoff et al., 2008; Sullivan et al., 2011; Arvidson et al., 2014). These experiments determined basic soil mechanics measurements of cohesion and angle of internal friction. Imaging and thermophysical properties and other relations were used to measure or constrain the particle size of the soils and the bulk density (e.g., Moore and Jakosky, 1989; Christensen and Moore, 1992; Herkenhoff et al., 2008; Golombek et al., 2008a).

Results of these experiments revealed four probable different soil deposits on Mars based on their mechanical properties and likely means of formation (e.g., Golombek et al., 2008a). Two types of deposits that appear to have been deposited by the wind were found at the landing sites. 1) Bedforms are composed of sand size particles that were sorted by the wind and include sand dunes and ripples. They are either well sorted by size or poorly sorted and typically cohesionless. Some of the ripples have a slightly cohesive near surface layer (few kPa) a few centimeters thick (Sullivan et al., 2011). 2) Drift deposits appear to be very fine grained dust (<10 μm) that has settled out of the atmosphere (Christensen and Moore, 1992; Moore et al., 1999; Paton et al., 2016). This material is also effectively cohesionless (and not load bearing). More cohesive soils have also been found. These soils have a cohesive surface

crust and/or break up into clods or blocks when deformed. Crusty and cloddy soils have cohesions of less than 4 kPa and blocky soils have higher cohesions of 3-11 kPa (Moore et al., 1987; Herkenhoff et al., 2008). Both are composed of dominantly sand size grains with some pebbles. The cohesive soils in most cases are limited to surface layers of the order of centimeters thick and likely formed by precipitation of salts from thin films of water interacting with the atmosphere (Haskin et al., 2005; Tosca et al., 2004; Hurowitz et al., 2006; Martın-Torres et al., 2015).

2.4 Internal Friction Angle

The internal friction angle of sands depends on their grain size distribution, grain shape, particle surface texture, grain arrangement and bulk density. Friction angles are determined by shearing specimens under constant confining stress, by using either a direct shear box or a triaxial apparatus. Shearing mobilizes irreversible volume changes. Loose sands decrease in volume due to the entanglement of grains during shear; dense sands increase in volume due to disentanglement, providing larger resistance to shear and higher friction angles. At the same density, angular particles provide higher friction angles than rounded particles. As discussed above, the surficial Martian regolith at the InSight landing site is expected to be composed of rounded particles in the range ~150-250 µm (fine sand) (Golombek et al., 2008a, 2017). In this regard, shear tests carried out on lunar regoliths (Scott, 1987) or lunar regolith simulants (JSC-1 simulant or other crushed basalts, e.g., McKay et al., 1994; Alshibli and Hasan, 2009; Vrettos, 2012) are not relevant, given the highly angular shape of their grains. As shown in Delage et al. (2017), various Mars regolith simulants, that have been apparently selected based on mineralogical considerations, are also somewhat angular. The Mojave Mars Simulant provided by JPL (MMS, Peters et al., 2008) is crushed Miocene basalt, the Mars Soil Simulant-Dust provided by DLR (MSS-D; Becker and Vrettos, 2016) is a 50/50 mix of crushed olivine and quartz sand (with a bimodal grain size distribution curve and olivine particles finer than what is expected at the InSight landing site). The Eifelsand simulant of DLR is a mix of crushed basalt and volcanic pumice sand (Delage et al., 2017). In this respect, simulants based on quartz sands (e.g., WF34; Lichtenheldt, 2016) may be mechanically more representative for what is expected to be present at the InSight landing site, as quartz sands show mainly rounded to sub-angular grains.

Lee and Seed (1967) considered changes in friction angle with density in a terrestrial Sacramento River (USA) sand, which is composed of rounded grains. These changes are compared in Figure 4 with the friction angles of a Mojave simulant (a mix of MMS, containing alluvial sedimentary and igneous grains

386 from the Mojave Desert and basaltic pumice), MSS-D, and Eifelsand, determined with a direct shear box
387 at a bulk density of 1570 kg/m^3 by Delage et al. (2017). The figure demonstrates the decrease in friction
388 angle at lower density with a good correspondence between the Sacramento River sand and the Mojave
389 simulant (angle of 38°, compared to 35° for MSS-D and 42° for Eifelsand, probably due to the very angular
390 and irregular shape of pumice particles). Extrapolation at bulk density of 1300 kg/m^3 provides a friction
391 angle between 28 and 30° for the surficial layer at the InSight landing site.

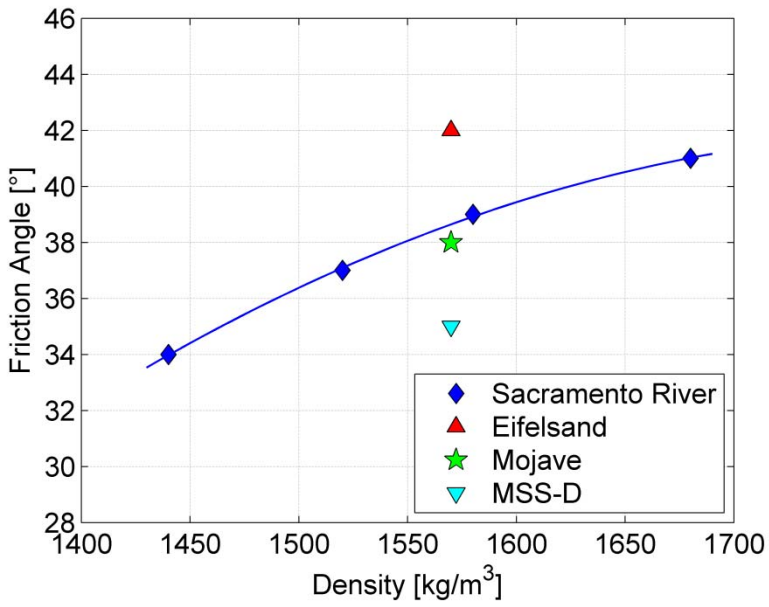

Figure 4: Change in friction angle with density of the Sacramento River sand (Lee and Seed 1967) compared to friction angles obtained with a direct shear box on various Mars regolith simulants by Delage et al. (2017). The Sacramento River sand has rounded particle that are closer in shape to Martian regolith than the simulants considered here. A friction angle around 28-30° is estimated at the surface of the InSight landing place. The changes in density with depth shown in Figure 3 provide a negligible increase at 5 m in the medium case, and an increase up to 36° in the very dense case.

392 The changes in friction angle with depth can be estimated based on the changes in density shown in
393 Figure 3, assuming a density dependence of the friction angle ϕ corresponding to that of the Sacramento
394 River sand. A second order fit to the data results in

$$\phi = A\rho^2 + B\rho - C \quad (2)$$

395 where ρ is given in units of kg/m^3. A, B, and C are constants with values of -5.9772 x 10^{-5}°m^6/kg^2,
396 0.21583°m^3/kg, and 152.88°, respectively. In the medium compacted case (Figure 3), the increase at 5 m
397 is negligible, whereas the friction angle increases up to 36° in the very dense case. As commented above,

398 the increase in density and friction angle also involves the mobilization of dilating behavior of the sand,
399 which could have some consequence on the penetrability of the mole. Dilation mobilized during
400 penetration at the sand/mole interface results in an increase in radial stress that makes the penetration
401 less efficient, as a greater portion of the stroke energy is needed to mobilize the soil.

402 ## 2.5. Grain size Distribution

403 We base our estimation of the average grain size distribution (GSD) within the InSight landing ellipse
404 using a combination of observations and modeling. We have previously used this approach to extrapolate
405 to the larger 10 cm particle size and hence determine the probability of obstruction of the HP^3 mole by a
406 rock (Golombek et al., 2017). Here we extend the extrapolation down to the smaller 600 µm, an upper
407 limit of the particles that may be present through eolian processes. The model parameters are derived
408 for the fragmentation that has produced the observable rocks through meteorite impact, and therefore
409 extrapolation into a size regime potentially dominated by eolian processes has limited justification.

410 Our previous study applied the negative binomial (NB) fragmentation model (Charalambous,
411 2014/2015) to the rocks of the compiled HiRISE images from the InSight landing ellipse (Golombek et al.,
412 2017). We validated this approach by matching rock distributions from HiRISE images of Viking 2, Mars
413 Pathfinder, Spirit, and Phoenix to subsequent ground truth imaging. We predicted that the surface
414 population down to 10 cm is likely to be similar to that observed at Columbia Memorial Station (CMS)
415 (Golombek et al., 2017). The NB model is readily able to extrapolate the particle size distribution of a
416 surface population used to validate the model down to 5 cm in the case of Spirit and Phoenix.

417 In estimating a cumulative mass fraction of the regolith, it is necessary to match both the surface rocks'
418 size distribution, and the rock coverage expressed as a cumulative fractional area (CFA). To match both
419 in general requires an adjustment, in this case an addition, of material below the observable rock size.
420 The physical basis for such an addition is deposition of eolian material and subsequent mixing by
421 meteorite impact. This dilution of the fragmentation products by eolian material provides the observed
422 CFA. The eolian material can only be introduced for particle sizes below the saltation limit which we take
423 at the upper limit of 600 µm. (Kok et al., 2012). Figure 5 shows the predicted grain size distribution (GSD)
424 based on these considerations down to the saltating upper size bound which, for the case of the InSight
425 landing site ellipse (E9), predicts the GSD ~75% by mass below 600 µm.

We can state that the GSD at the InSight landing site is likely to be close to the GSDs of the CMS and Phoenix landing sites, even though eolian processes might dominate at the InSight landing site. The thermal inertia in InSight landing ellipse has a value of about 200 J/(m^2 K s^{½}), similar to that of CMS and Phoenix landing site. As the thermal inertia is dominated by particles of 100 µm or below in size, this suggests a common eolian component. On this basis, the predicted grain size distribution for the InSight landing site is expected to make a transition below 600 µm to match the observed GSD of the sand determined by the Phoenix microscope station (Pike et al., 2011).

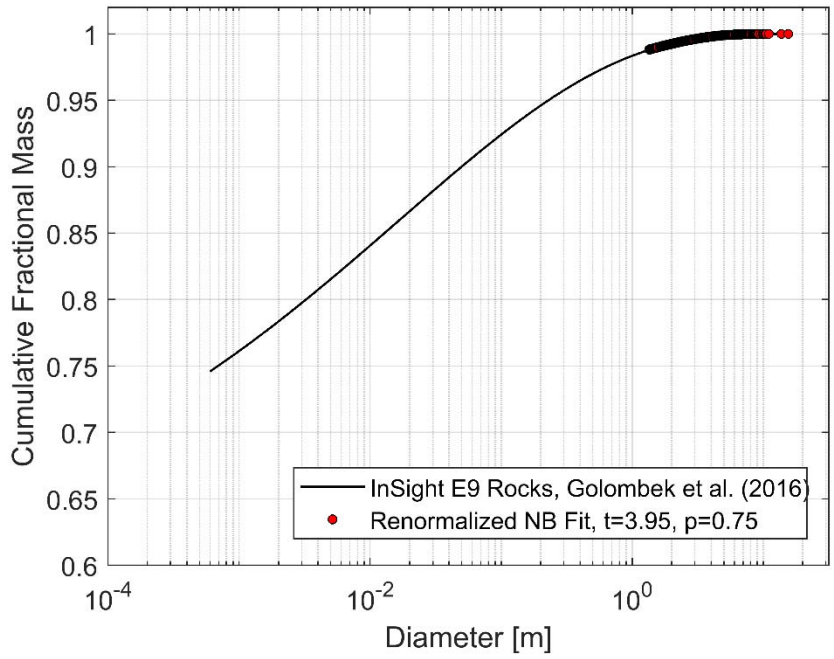

Figure 5: Plot of the cumulative fractional mass versus diameter of the rocks measured above the resolution limit at the InSight landing ellipse E9. The rocks are shown in red, while the negative binomial (NB) fit and prediction to the rock data distribution and below is shown in black. The mass estimation assumes spherical particles and constant density and it is renormalised to match the observable cumulative fractional area (CFA), as previously reported by (Golombek et al., 2017). The NB fit is extrapolated down to 600 µm – a reported upper size limit for saltation (Kok et al., 2012) – and estimates an approximate value of mass at 75% below this limit.

3. Regolith Thermophysical Properties

This section compiles regolith material parameters needed to calculate subsurface temperatures at the InSight landing site. The energy balance of the shallow subsurface is governed by insolation, regolith thermal inertia, and heat diffusion into the deeper subsurface. The one dimensional heat diffusion equation can be written as:

$$\rho(z)c_p(T)\frac{\partial T}{\partial t} = \frac{\partial}{\partial z}k(z,P,\rho,T,\sigma)\frac{\partial T}{\partial z} \quad (3)$$

where ρ is density, c_p is specific heat, T is temperature, z is depth, P is CO_2 gas pressure, t *is time*, σ is ambient (overburden) pressure, the pressure exerted by the gravitational attraction of the mass of the column of regolith above the depth of interest, and k is thermal conductivity. Equation (3) is a second order differential equation, which can be solved by prescribing two boundary conditions: One is usually given by constant (or zero) heat flux at a depth, while the other is usually given in terms of the surface energy balance. For periodic insolation forcing, the surface energy balance takes the convenient form

$$\sigma_B \varepsilon T^4 = (1-A)S + \varepsilon R + I\sqrt{\frac{\pi}{p}}\frac{\partial T}{\partial z'}\Big|_{z'=0} \quad (4)$$

where σ_B is the Stefan-Boltzmann constant, ε is surface emissivity, A is albedo, S is total solar radiative flux including scattered radiation, R is the thermal radiative flux from the atmosphere towards the surface, p is the period of the forcing, and $z' = z/d_e$ is depth normalized to the thermal skin depth $d_e = \sqrt{kp/\varrho c_p \pi}$. In Equation (4), all material parameters have been absorbed in the thermal inertia I, which is defined as

$$I = \sqrt{k\rho c_p} \quad (5)$$

Equation (5) is only valid when thermal conductivity is constant, which is not the case (see below). However, constant thermal inertia is a convenient way to describe the response of surface temperatures to insolation changes, and it is thus a widely used approximation. However, care must be taken when converting thermal inertia to material parameters like thermal conductivity, since different combinations of material parameters govern the temperature at the surface (thermal inertia) and in the subsurface

(thermal diffusivity, see below). The expected values of material parameters and their dependencies will be discussed for the InSight landing site below.

3.1. Surface Emissivity

Emissivity ε is defined as the ratio of emitted specific radiance I_r (W/(µm m^2 sr)) to the black-body radiance B of a surface at temperature T. Emissivity is a function of the wavelength λ and viewing angle, but the angle dependence is commonly assumed to be negligible and the radiative heat flux density q_{rad} $(\mathrm{W/m^2})$ of thermal emission can be represented via hemispherical integration as

$$q_{rad} = \pi \int_0^\infty \varepsilon(\lambda) B(T,\lambda) d\lambda \qquad (6)$$

Often, ε is assumed to be a constant, i.e., $\varepsilon = \varepsilon_q$, where ε_q is the weighted spectral average emissivity. Equation 6 can then be reduced to a form similar to the Stefan-Boltzmann Law:

$$q_{rad} = \varepsilon_q \sigma_B T^4 \,. \qquad (7)$$

where σ_B is the Stefan-Boltzmann constant. This approximation is usually sufficient for thermal models but has a systematic error as a function of T if ε varies with wavelength.

Instruments for Mars surface thermal emission observations include the Thermal Emission Spectrometer (TES) on Mars Global Surveyor (Christensen et al., 2001), the Thermal Emission Imaging System (THEMIS) on Mars Odyssey (Christensen et al., 2003a), the Mini-Thermal Emission Spectrometer (Mini-TES) on the Mars Exploration Rovers (Christensen et al., 2004a, b), the Planetary Fourier Spectrometer (PFS) on Mars Express (Formisano et al., 2005) and the Ground Temperature Sensor of the Rover Environmental Monitoring Station (REMS – GTS) on the Mars Science laboratory (Gomez-Elvira et al., 2012). It should be noted that interpretation of thermal emission is ambiguous because two unknowns, i.e., surface temperature and emissivity, contribute to the radiance, while only a single quantity is measured. Therefore, observations aim at measuring radiance close to the Christiansen wavelength, the wavelength at which the real part of silicate particle refractive index matches that of the atmosphere, and emissivity is close to unity (Conel, 1969).

Assuming soil physical and compositional properties similar to those observed at the two Mars Exploration Rovers landing sites (Golombek et al., 2005, 2008a; Yen et al., 2005), the InSight site is expected to be covered by basaltic sand, possibly covered in places with a fine, higher albedo dust. We

use Mini-TES spectra analyzed by Ruff et al. (2006) as a basis for emissivity estimates. These spectra are shown in Figure 6. They correspond to a bright dust drift (green), a basalt rock cleaned of dust by the Rock Abrasion Tool (blue), and to the darker sand exposed at surfaces disturbed by the rovers at Gusev crater (red) and Meridiani Planum (black). Data affected by the set of strong CO_2 absorption lines near 15 µm wavelength have been removed.

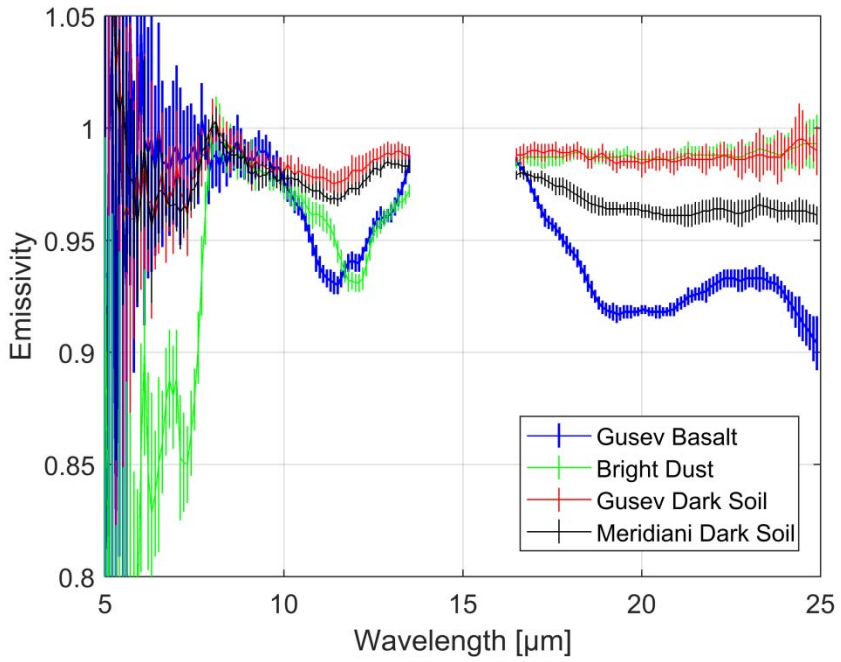

Figure 6: Emissivity spectra from the Spirit and Opportunity Mini TES instrument (Ruff et al., 2006). Blue: Gusev basalt (2t 131344843 emr 1151 p3175 n0 a1). Green: bright dust (2t 133288501 emr 2232 p3654 n0 a1). Red: Gusev dark soil (2t 130533990 emr 09 br p3156 n0 a1). Black: Meridiani Planum dark soil (1t 132362778 emr 05 am p3217 n0 a1).

The constant emissivity ε_q that best represents the heat flux from the surface is a function of composition and surface temperature, because the peak of the blackbody emission changes significantly within the range of expected temperatures. For the dark soil, the expected value for ε_q is in the range of 0.97 to 0.985, with less than 0.5 % change with temperature. The bright dust and basalt have a similar ε_q of 0.96 at 285 K, which increase by 2 % and decrease by 1.5 % towards 185 K, respectively. Therefore, based on remote sensing and in-situ data, a constant emissivity value of 0.98 (+1% /-2%) is suitable for both thermal modeling and surface temperature derivation at the InSight landing site, and the stated uncertainty is equivalent to a deviation in derived thermal inertia of <20 J/(m^2 K s$^{1/2}$) in the model of Vasavada et al. (2017). Examples of weighted average thermal emissivities for the HP^3 radiometer filters are given in Table 2.

Table 2: Weighted average emissivity for three wavelength bands corresponding to the HP^3 radiometer filters at 235 K for four different soils measured in-situ by the Mars Exploration Rover's Mini TES instrument.

	8 – 14 μm	8 – 9.5 μm	16 – 19 μm
Gusev dark soil	0.98	0.99	0.99
Meridiani dark soil	0.98	0.98	0.97
Bright dust	0.97	0.99	0.99
Gusev Basalt (Humphrey)	0.96	0.99	0.96

3.2. Surface Thermal Inertia

Thermal inertia describes the resistance to a change in temperature of the upper 2–30 cm of the surface. Fine particles change temperature quickly and therefore have low thermal inertia; higher thermal inertia surfaces are composed of sand, duricrust, rock fragments, or a combination of these materials. Bulk orbital thermal inertia observations of Mars include values derived from: (1) Viking Infrared Thermal Mapper (IRTM) data at ~60 km per pixel (Kieffer et al., 1977; Palluconi and Kieffer, 1981), (2) Mars Global Surveyor TES data (Christensen et al., 1992) at 8 pixels per degree (Mellon et al., 2000; Christensen et al., 2001) and at 20 pixels per degree (Putzig et al., 2005; Putzig and Mellon, 2007), and (3) Mars Odyssey THEMIS data at ~100 m/pixel (Christensen et al., 2004c; Fergason et al., 2006a; Fergason et al., 2012). Surface thermal inertia measurements were also obtained by the Miniature Thermal Emission Spectrometer (Mini-TES) on the Spirit and Opportunity rovers during their traverses (Christensen et al., 2003b; Fergason et al., 2006b). In addition, Curiosity determined thermal inertia from Ground Temperature Sensor (GTS) measurements from the Rover Environmental Monitoring Station (REMS) instruments (Hamilton et al., 2014, Vasavada et al., 2017).

Bulk thermal conductivity ranges over 3 orders of magnitudes on Mars as a function of the physical state of the (sub-)surface (compared to small factors for ρ and c_p as a function of the porosity, temperature, composition, etc., compare Equation (5)). I is virtually independent of the product $\rho c_{p,}$ whose value is generally close to ~10^6 J/(m^3 K) (Neugebauer et al., 1969; Fergason et al., 2006a), and is mainly controlled by k. More precisely,

$$k \approx \frac{I^2}{8 \cdot 10^5} \quad \text{W/(m K)} \tag{8}$$

for temperatures and surface densities at the InSight landing site. On Mars, thermal inertia values have largely been derived from remote measurements. Because of the strong dependence of its value on grain size and degree of cementation, Putzig (2006) distinguished between dust (28-135 J/(m^2 K s^{½})), sand (135-630 J/(m^2 K s^{½})) and duricrust (252-513 J/(m^2 K s^{½})). Paton et al. (2016) gave a value for I of 81 to 125 J/(m^2 K s^{½}) for dust around the Viking 1 footpads from direct measurements.

The highest resolution TES nighttime thermal inertia determination of the InSight landing site (Putzig and Mellon (2007) at 20 pixels per degree range from 138 to 284 J/(m^2 K s^{½}) and average 218 J/(m^2 K s^{½}) (n=314). A regional thermal inertia map (100 m spatial scale) was generated for the landing site (Golombek et al., 2017) from predawn temperature data acquired by THEMIS band 9 (12.57 μm) (Christensen et al., 2004c) between Mars Year 30 and 32 during low-dust seasons to minimize the atmospheric impact on the derived values. The resulting thermal inertia map displays values ranging from ~70 J/(m^2 K s^{½}) to 390 J/(m^2 K s^{½}), but 99% of the area has a thermal inertia of 130 to 220 J/(m^2 K s^{½}). Within the landing ellipse, the range is even smaller, demonstrating high thermophysical homogeneity at the 100 m scale over the entire landing region. The median regional thermal inertia is ~180 J/(m^2 K s^{½}), corresponding to cohesionless ~170 μm material (fine sand) based on laboratory work and theoretical relationships (Presley and Christensen, 1997a; Piqueux and Christensen, 2011). Higher thermal inertia values are expected to be associated with medium to coarse sand, and will likely include mixtures of grain sizes, including larger clasts such as those surfaces observed at Gusev crater (Golombek et al., 2005, 2008a; Fergason et al., 2006b). The corresponding diurnal skin depth values (i.e., depth at which maximum amplitude is attenuated to 37% of its surface amplitude) is a maximum of ≤6 cm, indicating that the upper few cm of the surface layer are characterized by these thermal inertia values. The lack of seasonal variations in thermal inertia indicates that the same thermal inertia and materials extend a few tens of cm below the surface (Golombek et al., 2017).

The lowest thermal inertia values in the landing region (e.g., ~70 J/(m^2 K s^{½})) are rare, and typically are observed within depressions probably that trap atmospheric dust and very fine sand, or on the lee side of positive topographic features (Golombek et al., 2017). These low inertia values could result from fine sand (100–200 μm) with a very thin coating (<1–2 mm) of dust (several μm diameter particles). The highest thermal inertia values (i.e., 350–390 J/(m^2 K s^{½})) are also uncommon, associated with crater rims and ejecta blankets, as expected for rocky ejecta craters, but not bedrock at the 100 m spatial scale.

Regolith induration is not inconsistent with the derived thermal inertia values, however thermal modeling of cemented regolith shows that the volume of the cementing phase would need to be minimal (e.g., typically <0.1% in volume) with little impact on the mechanical properties (Piqueux and Christensen, 2009a). Comparison of the cohesion of surface soils at other landing sites with their thermal inertia would limit the cohesion to less than a few of kPa, consistent with very weakly bonded soils on Earth (Golombek et al., 1997, 2008a).

3.3. Surface Albedo

The albedo, or surface reflectivity or brightness of reflected solar energy from the surface in which the viewing geometry has been taken into account, has been measured globally by both IRTM and TES at 1 pixel and 8 pixels per degree, respectively (e.g., Pleskot and Miner, 1981; Christensen et al., 2001). The albedo can, for example, be used to infer the dustiness of the surface, as very dusty areas exhibit very high albedo (and, in addition, very low-thermal inertia) (Christensen and Moore, 1992; Moore and Jakosky, 1989; Mellon et al., 2008; Putzig et al., 2005; Golombek et al., 2008a). The amount of dust cover at the landing sites was also evaluated using the TES dust cover index (16 pixels per degree), which includes a more explicit measure of the particle size and the amount of dust coating the surface (Ruff and Christensen, 2002).

The albedo of the InSight landing site is about 0.25 from IRTM (Pleskot and Miner, 1981) and 0.24 from TES (Christensen et al., 2001). This relatively high albedo is consistent with atmospherically deposited dust, which is consistent with its relatively high dust cover index (Ruff and Christensen, 2002). However, thermal inertia values are nowhere dominated by very fine material at the 100 m scale suggesting that dust may form an optically thick but thermally thin coating (hundreds of μm) on most surface materials in this region of Mars. This interpretation is supported by the similarity of the dust cover index in the InSight landing site region (0.94) with the Viking Lander 2 site and dusty locations of the Gusev cratered plains explored by Spirit (e.g., Golombek et al., 2005, 2006), both of which had very thin dust coatings.

All previous landers on Mars have modified the surface during landing (e.g., Moore et al., 1987; Golombek et al., 1999; Squyres et al., 2004; Soderblom et al., 2004; Smith et al., 2009; Arvidson et al., 2014; Daubar and McEwan, 2015). The InSight lander will use pulsed retropropulsive thrusters to slow itself during landing. The thrusters on InSight are the same as those used by the Phoenix lander, which dispersed 5-18 cm of soil exposing water ice when landing (Mehta et al., 2011). Modeling of this process showed that pulsed thrusters lead to explosive erosion via cyclic shock waves that fluidize soils, producing

ten times greater erosion than conventional jets (Mehta et al., 2011, 2013). Consideration of these effects for InSight landing indicates that generally circular depressions will form at the jet impingement locations, but they will not be large enough to appreciably alter the surface topography at the lander footpad locations and thus won't pose a risk to landing safely (Golombek et al., 2017). Nevertheless, surface soils will be dispersed away from the lander with sand and pebbles being eroded from the jet impingement locations and deposited away from the spacecraft.

The thin coating of fine-grained dust present at the landing site will be dispersed into the atmosphere at the time of landing, reducing the albedo of the surface around the lander. This has been observed to occur around previous landers, and in the cases of Phoenix and Mars Science Laboratory (Curiosity) the effect can be measured using relative albedo measurements in HiRISE images (Daubar and McEwan, 2015). The quantity of albedo change and rate of subsequent brightening varied depending on the particular piece of hardware; for the MSL descent stage, the albedo was initially lowered by ~50%. After the initial darkening, images show a rapid initial brightening that slowed over time, following a logarithmic function. The majority of the blast zone faded to ~90% of the initial albedo by ~500 days after landing, but the darkest areas have not faded completely. Although it is located at high latitudes, the Phoenix landing site is in some ways a better analogy for InSight due to the same landing thrusters; however, monitoring of the Phoenix site is complicated by seasonal activity and limitations to orbital observations. The Phoenix landing reduced the surroundings to ~60-80% of the pre-landing albedo. Before subsequent orbital images could be taken in the same season, the blast zone disappeared, presumably due to seasonal frosts redistributing surface dust.

Based on these observations and the relatively dusty nature of western Elysium Planitia, we would expect similar changes to the InSight landing site, where the surface albedo can be expected to be reduced by ~20-50% upon landing, then exhibit a rapid initial brightening, and then gradually return to the surrounding albedo over the next several Mars years. The reduction in albedo will warm the surface and the deposition of sand and pebbles from the thrusters could also have a thermal effect.

3.4.Thermal Conductivity

This section describes recommended values for the thermal conductivity *k* of the regolith expected at the InSight landing site, based on orbital data and published laboratory/theoretical work. Unless otherwise specified, the regolith is treated as an idealized discontinuous medium composed of spherical basaltic grains in stagnant CO_2 gas. The relationship between bulk regolith conductivity and various

605 controlling factors (i.e., pressure, temperature, grain size, porosity, etc.) is quantitatively described in the
606 literature for a wide range of planetary configurations of atmospheric pressures, compositions, regolith
607 properties, etc. For the specific case of the InSight landing region, these relationships have been tailored
608 to the expected subsurface properties for simplicity, and are presented here. We will first discuss an
609 appropriate choice for the simple case of constant thermal conductivity and then present the more
610 general case of temperature and depth dependency.

611 Thermophysical properties of the landing region have been characterized from orbital data acquired
612 by the Thermal Emission Imaging System (THEMIS) (Christensen et al., 2004c). In the landing ellipse,
613 thermal inertia *I* values derived from temperature measurements typically range from 130 to 220 J/(m^2 K
614 $s^{1/2}$) with a median value of ~180 J/(m^2 K $s^{1/2}$) (Golombek et al., 2017). Using relationships established in
615 the laboratory (Prelsey and Christensen, 1997b) the expected regolith thermal conductivity is 0.017 < *k* <
616 0.048 W/(m K) with median value of 0.032 W/(m K) corresponding to ~150-170 µm unconsolidated grains
617 (Golombek et al., 2017).

618 Published thermophysical studies of Martian subsurface temperatures generally use fixed *I* or *k* (as
619 opposed to temperature or pressure-dependent values), because these dependencies are not
620 straightforward to determine, and because they result in small overall conductivity (Piqueux and
621 Christensen, 2011) and surface temperature (Kieffer, 2013) changes at the expense of longer processing
622 time. In the context of the InSight heat-flow experiments. However, subtle conductivity variations may
623 need to be accounted for. Therefore, the dependence of thermal conductivity on gas pressure,
624 porosity/density, temperature and overburden pressure/stress will be considered in this section.

625 Because of the discontinuous nature of the solid phase, with inter-grain regions impeding the flow of
626 heat from grain to grain, the bulk regolith conductivity is strongly influenced by the pore-filling CO_2 gas
627 conductivity (~0.01 W/(m K) at 220K). In rarefied gas environments, where the mean free path of gas
628 molecules is similar to the volume that encapsulates them (i.e., the pore space) as is the case in the
629 Martian regolith, small pressure variations can result in noticeable bulk conductivity changes. Laboratory
630 experiments have quantified this effect (Fountain and West, 1970; Presley and Christensen, 1997a), and
631 numerical models also include it (Piqueux and Christensen, 2009b). The effect of gas pressure on the bulk
632 conductivity is described by the empirical Equation 9 (modified from Presley and Christensen, 1997b):

$$k = (CP^{0.64})d^{-0.125\log(\frac{P}{K})} \quad (9)$$

633 with C = 0.001262, K = 107990 hPa , d is the grain diameter in µm, and P is pressure in hPa. This equation
634 is dimensionally unbalanced and was derived by Presley and Christensen (1979b) from log-log plots of
635 laboratory measurements of thermal conductivity as a function of gas pressure for different grain sizes in
636 the range of 11 to 900 µm. The equation is not based on a theoretical analysis of heat transfer in granular
637 media. Figure 7 shows the predicted variation of the bulk conductivity as a function of the atmospheric
638 pressure using Equation (9). For a given location, the ~30% seasonal variation of the atmospheric pressure
639 due to the CO_2 cycle at the poles (Leighton and Murray, 1966; Hess et al., 1979) induces ~10% of
640 conductivity variation. A simplification of Equation (9) gives (Figure 10):

$$k(P + \Delta P) = k_0(P) \cdot (1 + A \cdot \Delta P + B \cdot \Delta P^2) \quad (10)$$

641 where $k(P + \Delta P)$ is the thermal conductivity at a pressure with ΔP the atmospheric pressure deviation
642 (in hPa) from the local mean pressure P and $k_0(P)$ the nominal regolith conductivity at pressure P. A =
643 5.173 hPa^{-1} and B = -2.416 10^{-1} hPa^{-2} are coefficients derived from a fit based of Equation (10) and Figure
644 7. Coefficients in Equations 9 and 10 are only valid for the range of range of grain sizes and pressures
645 used in the Presley and Christensen (1979b) laboratory experiments.

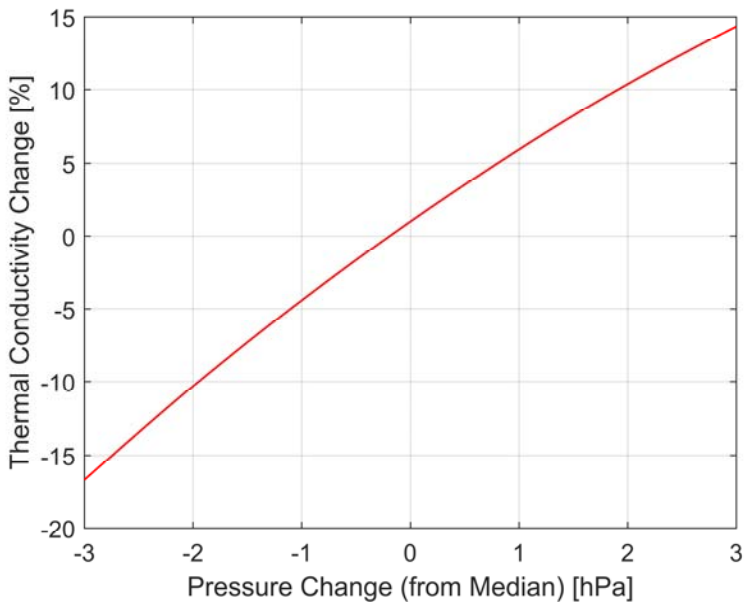

Figure 7: Relationship between thermal conductivity change and atmospheric pressure based on data from Presley and Christensen (1997b).

In addition, we note that Equations 9 and 10 do not apply for strongly cemented material. With indurated material, the relatively low pore-filling gas conductivity that enables heat transfer in the high impedance inter-grain region is replaced by high-conductivity inter-granular material (solids such as salts or ices are several orders of magnitude more conductive than rarefied CO_2 gas) and control the dependence of k on the temperature and pressure (Piqueux and Christensen, 2009b). As a result, the bulk thermal conductivity of cemented regolith is less dependent on atmospheric pressure variations. Equation 10 only provides an upper limit to the dependence on pressure. We note that the interpretation of remote sensing thermal infrared data is not consistent with a fully encrusted regolith, but does not exclude a very slight surface induration (Golombek et al. 2017). We anticipate Equation 10 to be adequate in the nominal landing region.

Laboratory experiments (Fountain and West, 1970; Presley and Christensen, 1997a) and theoretical considerations (Piqueux and Christensen, 2009b) indicate that the porosity of the Martian regolith partially controls the bulk thermal conductivity. High porosities are generally associated with lower bulk conductivities.

Fountain and West (1970) (their Figure 3) used samples typically finer than those expected at the InSight landing site (i.e., 37-62 µm), and they found an ~200+% increase in bulk conductivity for a ~50% increase of the density (ignoring their very low density samples). Based solely on numerical modeling, Piqueux and Christensen (2009b) found a doubling of the bulk conductivity associated with a doubling of the density (their Figure 7). Presley and Christensen (1997b) observed a ~30% increase of the bulk conductivity for a 30% increase of the density for Kyanite samples at all pressures tested, a trend consistent with modeling by Piqueux and Christensen (2009b), but significantly less pronounced than that by Fountain and West (1970). We propose to adopt a linear conductivity dependency on density that conforms with the most recent laboratory work models (i.e., work by Presley and Christensen (1997b), and Plesa et al. (2016)):

$$k(\rho+\Delta\rho) = k_0(\rho) \cdot (1 + 0.005 \cdot \Delta\rho) \quad (11)$$

where $k(\rho+\Delta\rho)$ is the thermal conductivity with $\Delta\rho$ the change in regolith density (in %) from the nominal density ρ, and $k_0(\rho)$ the conductivity with the nominal density.

Under most Martian surface conditions, including those expected at the InSight landing site, although radiative heat transfer probably dominates in the atmosphere (e.g., Martinez et al., 2014) it is small

compared to other mechanisms in the regolith (Vasavada et al., 1999) and is therefore ignored in the analysis here. Apart from radiative heat transport, temperature also controls the pore-filling gas conductivity, as well as the solid phase conductivity. The solid phase conductivity is only weakly linked to the bulk regolith conductivity, such that temperature induced variations of the solid phase conductivity can usually be ignored.

A theoretical quantification of the bulk conductivity dependency on the gas conductivity is a difficult problem because of the complex geometry of the gaseous phase and its relationship to the solid phase. Increasing the regolith temperature increases the intrinsic conductivity of the pore filling gas (Vesovic et al., 1990), but also decreases the mean free path, reducing the efficiency of the gaseous heat transfer. A quantitative comparison of these two opposite mechanisms requires numerical modeling and indicates that the reduction of the mean free path has a very small effect compared to the general bulk gas conductivity increase with temperature (Piqueux and Christensen, 2009b; 2011). As a result, increasing the temperature in stagnant CO_2 gas and with pressures consistent with Mars increases the bulk conductivity of the regolith, as confirmed by laboratory measurements (Fountain and West, 1970). Piqueux and Christensen (2011) compared the temperature effect on k predicted by their model with the data published by Fountain and West (1970), and results are shown in Figure 8.

Generally, the numerical model predicts a larger temperature-dependency than observed in the laboratory, over a wide range of material density and temperatures. While Fountain and West (1970) do not formally provide a relationship between temperature and bulk conductivity, their data indicates a ~15-20% increase in bulk conductivity over 100K (Figure 8), in line with the expected increase in pore-filling gas conductivity over this range of temperatures. For comparison, a Piqueux and Christensen (2011) model emulating these laboratory conditions found a ~30% increase over 100K (Figure 8), which is remarkably close to the experimental observations given the numerous modeling assumptions. Given that the temperature dependence of the pore fill gas is the major contribution to the thermal change, we propose as square-root dependence of regolith thermal conductivity on temperature, consistent with the kinetic theory of gases. Bulk conductivity as a function of temperature $k(T)$ where T is temperature (in K) is then given by

$$k(T) = k_0(T_0)\sqrt{T/T_0} \tag{12}$$

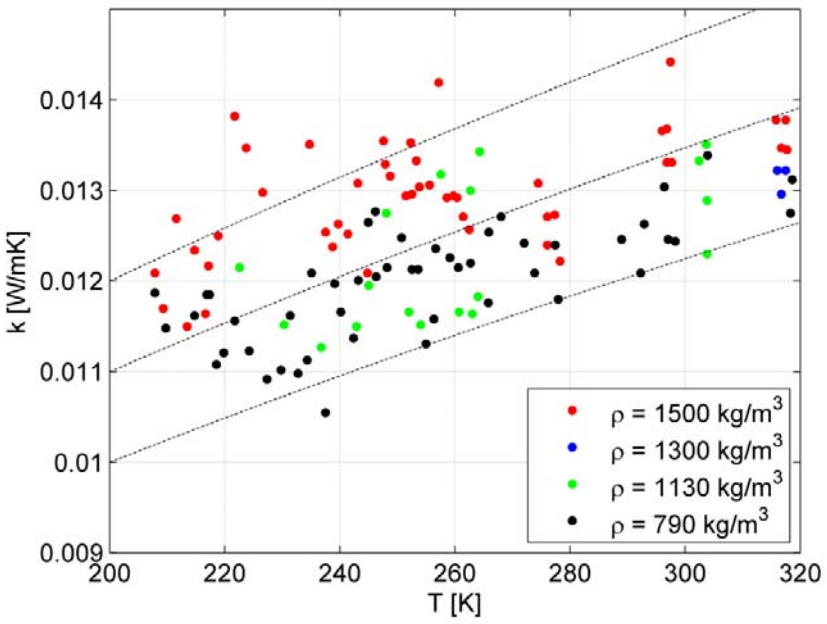

Figure 8: Comparison between thermal conductivity measurements of 37–62 µm particles of basalt under 7 hPa of CO_2 gas as a function of the temperature by Fountain and West (1970) (dots) and thermal conductivity trend modeled using Equation 6 (dashed lines).

where T_0 and k_0 are the nominal temperature (in K) and regolith conductivity (in W/m K), respectively. A fit to the data by Fountain and West (1970) is shown in Figure 8, demonstrating that this approximation is appropriate for the range of temperatures expected to be encountered on Mars. Again, this trend only applies for unconsolidated material in the presence of rarefied gas. In the case of a duricrust, Equation 12 does not apply because the gas conductivity does not dominate the bulk conductivity, and the thermal conductivities of solid (cementing) phases generally decrease with increasing temperature, following a trend opposite to Equation 12. As a result, the dependence of *k* with *T* in the case of indurated material is nonlinear and too complicated to predict without ad hoc models (Piqueux and Christensen 2011).

An increase of the confining pressure, for example as a result of the progression of the HP^3 mole, is expected to result in an increase of the bulk regolith conductivity by increasing the contact area between grains (Hertz, 1895), hence facilitating the flow of heat from grain to grain at the expense of the relatively inefficient (but dominating) gaseous heat transfer. Elasticity theory suggests that contact area, and thus thermal conductivity, should scale with stress σ to the power of one third, but different scaling relations with other power law dependence have also been suggested (e.g., Pilbeam and Vaisnys, 1973). However, current laboratory data is most consistent with a power law scaling close to the classical value, and

$$k = k_0 \left(\frac{\sigma}{\sigma_0}\right)^{1/3} \quad (13)$$

has been established for monodispersed spheres as well as for lunar analogue material (Sakatani et al., 2016), where k_0 is the conductivity at pressure σ_0.

Apart from the action of the HP^3 mole, stress anisotropy of the regolith itself could have an influence on regolith thermal conductivity. Stress anisotropy is generally described in terms of the dimensionless coefficient of lateral stress

$$K_0 = \frac{\sigma_h}{\sigma_v} \quad (14)$$

where σ_h and σ_v are the stresses in the horizontal and vertical directions, respectively. For normally consolidated soils, K_0 is usually between 0.4 and 0.5, consistent with Jaky's formula K_0 = 1-sin(ϕ) (Jaky, 1944) for angles of internal friction ϕ close to 30°. Stress anisotropy may then introduce anisotropy into the thermal conductivity, i.e., conductivity may vary between the horizontal and vertical directions. While this effect may be pronounced on airless bodies, it will be largely mitigated on Mars by the pore filling CO_2 gas.

In order to estimate the magnitude of the expected effect, the contribution of the pore filling gas to the total thermal conductivity can be estimated by writing $k_{h,v} = k_{sol,h,v} + k_{gas}$, where k_{sol} and k_{gas} are the solid and gas conductivity part of the thermal conductivity, and subscripts *h* and *v* refer to the horizontal and vertical direction, respectively. Using Equations (13) and (14), thermal conductivity in the horizontal direction can then be expressed as

$$k_h = k_{sol,v} {K_0}^{1/3} + k_{gas} \quad (15)$$

Hütter et al. (2008) give thermal conductivities of 0.008 and 0.057 W/(m K) for 100 – 200 µm diameter glass beads under vacuum and 8 hPa pressure conditions, respectively, and we therefore assume k_{gas} = 0.049 W/m K) and $k_{sol,v}$ = 0.008 W/(m K) respectively. Note that these grain sizes closely correspond to the expected grain size range at the InSight landing site derived from surface thermal inertia, which results in 150 µm diameter grains. Then, for normally consolidated soil, K_0 = 0.5 and k_h is expected to be smaller than k_v by about 2-3%. Note that this effect is even less pronounced for larger grain sizes, and can likely be ignored in the context of the InSight mission.

3.5. Specific Heat

The specific heat of rocks and soils at low temperatures has been studied for lunar samples (Robie et al., 1970; Fujii and Osako, 1973; Hemingway et al., 1973), and a strong temperature dependence has been found. The suite of materials studied includes particulate material such as lunar fines and soils, but brecciated lunar rocks as well as basalts have also been studied. A best fit to the lunar soils data was given by Hemingway et al. (1973) and the specific heat can be approximated as

$$c_P = -A + BT + CT^2 - DT^3 + ET^4 \quad (16)$$

where c_p is specific heat in units of J/(kg K), and A, B, C, D, and E are constants with values 23.173 J/(kg K), 2.127 J/(kg K^2), 1.5008 x 10^{-2} J/(kg K^3), 7.3699 x 10^{-5} J/(kg K^4), and 9.6552 x 10^{-8} J/(kg K^5), respectively, and T is temperature in K. This best fitting formula is accurate to within 2 percent down to 200 K and to within 6% down to 90 K. The fit is shown along with the data in Figure 9.

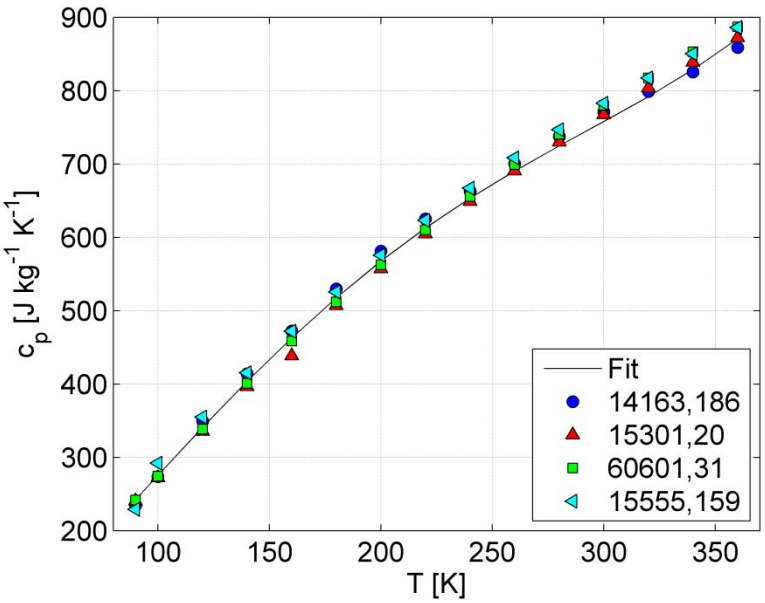

Figure 9: Specific heat of lunar samples 14163,186 (fines >1 mm, blue), 15301,20 (soil, red), 60601,31 (soil, green), and 15555,159 (basalt, cyan) as a function of temperature together with the best fitting curve (solid line). Data and fit from Hemingway et al. (1973).

Measurements on lunar material are in good agreement with a thermophysical model of Winter and Saari (1969), measurements on the physical properties of meteorites performed by Yomogida and Matsui (1983), and meteorite specific heat measurements by Consolmagno et al. (2013). It may be worth noting

752 that a trend exists with respect to the iron content of the samples, with low iron corresponding to high
753 specific heat (Yomogida and Matsui, 1983). The contribution of the gas phase to the bulk specific heat of
754 a soil is negligible when compared to the solid phase and is usually ignored (Piqueux and Christensen,
755 2011).

756 While specific heat thus shows a strong temperature dependence, this is only relevant if the near
757 surface regolith layer is considered. At depths below a few tens of cm, near surface temperature
758 perturbations rapidly decay (e.g., Grott et al., 2007; Kieffer, 2013) such that the regolith can be assumed
759 isothermal for the purpose of determining its specific heat. For the InSight landing site, average regolith
760 temperatures vary between 220 and 240 K (Plesa et al., 2016), corresponding to specific heat values of
761 612 and 653 J/(kg K) such that c_p = 630 J/(kg K) may be assumed.

762 3.6. Thermal Diffusivity

763 Thermal conductivity and specific heat are the most useful quantities in terms of modeling thermal
764 fluxes in the regolith and are probably the most physically meaningful. In practical applications, however,
765 they are often replaced by derived quantities that are either directly measurable or convenient shorthand
766 in equations. Apart from thermal inertia, which describes the reaction of surface temperatures to
767 harmonic temperature forcing and was introduced in section 3.2, thermal diffusivity can be used to
768 describe heat diffusion in the subsurface. Thermal diffusivity κ is defined as

$$\kappa = k/(\rho c_p) \quad (17)$$

769 where k is thermal conductivity, ρ is density, and c_p is specific heat. It is a particularly useful quantity if
770 material parameters can be assumed to be constant, and in this case the heat diffusion equation (Equation
771 3) takes a particularly convenient form. As can be seen from Equation (17), an increase in thermal
772 conductivity has the effect of a corresponding decrease in specific heat, which implies that thermal
773 diffusivity is somewhat less sensitive to changes in density (which is most sensitive to porosity in the
774 regolith) than thermal conductivity. Over a narrow temperature and depth range, κ can therefore be
775 approximated as a constant, thus facilitating analytical solutions of the heat conduction equation. It is
776 worth noting that estimates of thermal diffusivity from the attenuation of the diurnal temperature wave
777 on the Moon did not show any systematic effects below a depth of 50 cm (Langseth et al., 1976), and this
778 may be a valid approximation for the Martian subsurface as well. In this case, $\kappa = 3.6 \times 10^{-8}$ m^2/s would be
779 a reasonable estimate at the InSight landing site.

For planetary regoliths in general, it is the thermal conductivity whose effect dominates the behavior of κ which on Mars can span two orders of magnitude and be strongly temperature-dependent, whereas the range of both density ρ and specific heat c_p are usually rather narrowly constrained. If depth dependence of thermal diffusivity is deemed to be important, appropriate values for $\kappa(P, \rho, T, c_p(T))$ can easily be computed by inserting Equations 10, 11, 12, and 16 into Equation 17.

4. Regolith Elastic Properties

This section deals with the elastic properties of the regolith, which characterize its influence on the seismic wavefield as recorded by the SEIS (Seismic Experiment for Interior Structure) instrument. The relevant parameters discussed here are compressional wave velocity v_P, shear wave velocity v_S, Poisson's ratio ν which can be derived from these velocities, elastic modulus E which can be expressed in terms of the above quantities and density ρ, as well as the seismic quality factor Q.

4.1. Seismic Velocities and Poisson's ratio

Poisson's ratio ν describes the relation between transverse strain $\varepsilon_\perp$ and axial strain $\varepsilon_\parallel$ when a uniaxial stress is applied

$$\nu = -\frac{d\varepsilon_\perp}{d\varepsilon_\parallel} \tag{18}$$

It is directly related to the seismic P- and S-wave velocities v_P and v_S by

$$\nu = \frac{\left(\frac{v_P}{v_S}\right)^2 - 2}{2\left(\left(\frac{v_P}{v_S}\right)^2 - 1\right)} \tag{19}$$

with higher values of ν related to smaller shear resistance, and higher v_P / v_S.

In contrast to thermophysical properties, for which estimates can be based on remote sensing data from Mars, or other mechanical properties, for which data are available from other Martian landing sites, there are currently no in situ measurements of seismic velocities of the Martian regolith. Estimates thus

800 have to be based on laboratory experiments with analogue materials on Earth while also considering field
801 and lab data gathered for lunar regolith and terrestrial sands.

802 Both v_P and v_S were determined by Delage et al. (2017) for three Martian regolith soil simulants
803 under various confining pressures corresponding to lithostatic stresses from 5 m to more than 60 m
804 depth on Mars. The Mojave simulant, provided by JPL, is a mixture of MMS simulant, containing alluvial
805 sedimentary and igneous grains from the Mojave Desert, with basaltic pumice. The Eifelsand simulant
806 from DLR is a mixture of crushed basalt and volcanic pumice sand. The MSS-D simulant, also from DLR,
807 is an artificial sediment made of a 50/50 mixture of crushed olivine and quartz sand, with a bimodal
808 grain-size distribution, and olivine particles smaller than expected at the InSight landing site. As the
809 MSS-D particles are in the silt-size range (50% of particles smaller than 70 μm, and as small as 2 μm),
810 much finer than the particle sizes estimated for the regolith at the landing site (Golombek et al., 2017),
811 and are angular rather than rounded, the results more relevant to the InSight landing site are those for
812 the Mojave and Eifelsand simulants. The ejecta that form the Martian regolith are expected to be
813 rounded due to long term exposure to wind action in low atmospheric pressure conditions, in contrast
814 to lunar regolith particles that are not submitted to any wind and, as a result, are more angular. The
815 Mojave simulant contains both rounded and more angular grains and their particle size distribution is
816 closer to the landing site estimates, at least when using only particles smaller than 2 mm, as was done in
817 the laboratory measurements.

818 During the laboratory tests on Mojave simulant, Delage et al. (2017) observed no effect of stress cycles
819 on the values of seismic velocities, and hence no difference between the effect of either plastic (first stress
820 application) or elastic response along the compression strain. They found that the increase in velocity
821 was more sensitive to the increase in inter-granular forces resulting from an increase in confining stress,
822 and, to a lesser extent, to the corresponding increase in density. Data along three successive stress paths
823 as well as from tests carried out on two different samples showed good agreement. The smallest confining
824 stress used in these tests was 25 kPa, which approximately corresponds to 5 m depth on Mars, so the
825 properties of the regolith at shallower depth have to be extrapolated.

826 For all regolith simulants, a power-law increase of velocities with depth was observed, defined in
827 relation to confining stress σ_0' (in kPa) by an empirical law (Santamarina et al., 2001) given as:

$$v = \alpha \left(\frac{\sigma_0'}{1\ kPa} \right)^{\beta} \quad (20)$$

and where α and β are experimentally determined. α is the velocity of the velocity of the material subjected to 1 kPa confinement; β is non-dimensional.This kind of velocity-depth dependence is also common for terrestrial soils (e.g., Faust, 1951; Prasad et al., 2004). Fitting the laboratory measurements for v_P resulted in a value of 0.3 for the exponent β and, using the velocity values of 250 m/s at 25 kPa and 600 m/s at 500 kPa, a value of α = 95 m/s for the compressional velocity at 1 kPa confining stress. Surface velocities are derived assuming an atmospheric pressure of 0.6 kPa, and 81.5 m/s and 48.8 m/s for P- and S-waves, respectively. Theoretical estimates based on contact theory result in values of 1/6 for β for Hertzian contacts between elastic spheres and 1/4 for cone to plane contacts (expected for rough to angular particles) as well as for spherical particles with yield. Observed values for β for terrestrial sands vary from 1/3 to 1/6 (e.g., Zimmer et al., 2007).

Calculating the increases of confining stress with depth corresponding to the three density curves presented in Figure 3 leads to three corresponding velocity-depth profiles (Figure 10). However, differences between the three profiles are barely distinguishable, which is to be expected given the reported limited influence of density on the velocity increase with depth.

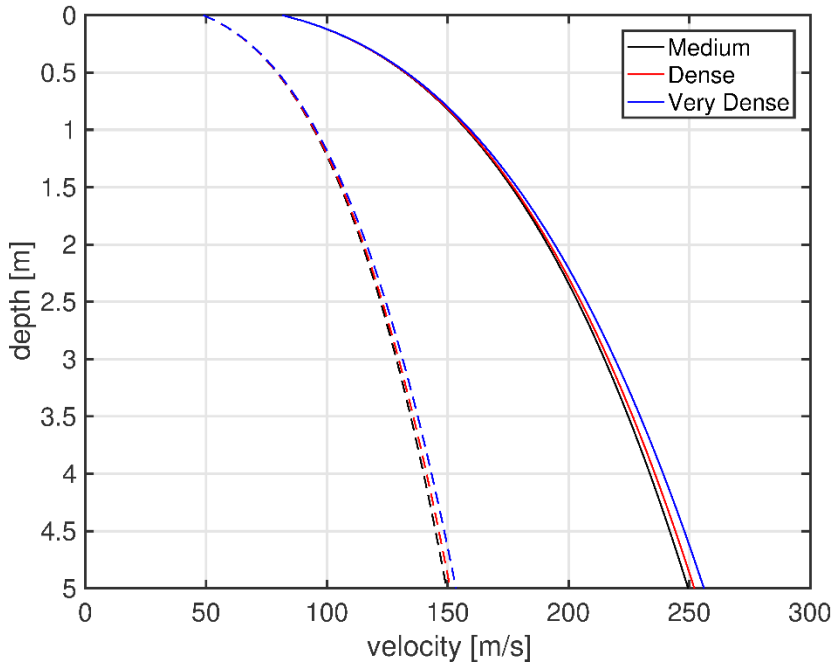

Figure 10: Model P- and S-wave velocities as a function of depth for the upper five meters of regolith at the InSight landing site. The three profiles correspond to the density profiles shown in

0.5 0.6 0.7 ρ_B 0.8 0.9

Equation 20 and the velocity measurement on the Mojave simulant have already demonstrated an important application in modeling the different seismic noise sources that may affect the InSight seismometers at various frequencies (Mimoun et al., 2017), although strictly speaking this model is only sensitive to the shear modulus and Poisson's ratio as the model is mostly integrating noise sources from static loading. For example, atmospheric pressure fluctuations on Mars induce an elastic response in the ground creating ground tilt, detectable as a gravity signal on the InSight seismometer SEIS. The amplitude of this pressure noise depends on the shear modulus and Poisson's ratio of the ground that are related, and may be derived from the seismic velocities and an assumed bulk density (Murdoch et al, 2017a). A further example is dynamic pressure due to wind that results in stresses on the InSight lander body and leading to ground deformation at the lander feet (Murdoch et al., 2017b). To calculate the resulting ground deformation at the seismometer's ground position for a given wind dynamic pressure and direction, local elastic properties beneath each foot of the lander are required. Seismic velocities may be obtained from equation 20 by taking into account the pressure exerted by the lander mass under Martian gravity and the elastic properties (shear modulus and Poisson's ratio) can then be derived. The noise maps produced by Murdoch et al. (2017b), based on these calculations, will assist in deploying SEIS at a site with little noise due to wind-induced ground deformation generated by the lander.

For v_S, no relation corresponding to Equation (20) was derived by Delage et al. (2017). However, it was found that the ratio between v_P and v_S remained rather constant for different confining stresses and for the different simulants tested. Thus, the values of v_S shown in Figure 10 are derived from v_P using the measured ratio of 1.669. The Poisson's ratio ν calculated via Equation (19) accordingly is 0.22 (Delage et al., 2017).

The velocity profiles in Figure 10 assume that the regolith is composed purely of sandy material. Rock abundance at the landing site is low (see section 1.2), though, and a fraction of 5% or 10% rocks would increase velocities v_P and v_S by less than 0.5% and less than 1.25%, respectively, for all three models. This estimate is based on using the Reuss average, as in Delage et al. (2017), and assuming rock properties of v_P = 3000 m/s, v_S = 1700 m/s and ρ = 2760 kg/m^3 derived from terrestrial data obtained for fractured basalt (Planke et al., 1999; Vinciguerra et al., 2005; Stanchits et al., 2006; Fortin et al., 2011) as well as a negligible influence of compression on the rocks within the upper 5 m of the regolith. An example of extending the velocity model to greater depths to include the coarse ejecta layer and the transition from fractured to pristine basalt can be found in Knapmeyer-Endrun et al. (2017).

872 Terrestrial lab measurements on unconsolidated dry quartz sand result in P-wave velocities around
873 250 m/s and S-wave velocities around 150 m/s for confining stresses below 50 kPa (e.g., Velea et al., 2000;
874 Zimmer et al., 2002; Prasad et al., 2004). A terrestrial field experiment on soil with a low water content
875 yielded P-wave velocities as low as 150 m/s and S-wave velocities as low as 100 m/s directly at the surface
876 (Uyanik, 2010), whereas field measurements on beach sand showed P-wave velocities as low as 40 m/s
877 and an average of 160 m/s above the water table at 1.4 m depth (Bachrach et al., 1998). A summary of
878 terrestrial field results from exploration studies also finds P-wave velocities around 200 m/s in shallow
879 soils (Ohsaki and Iwasaki, 1973). Thus, the regolith velocity models are within the range observed for
880 terrestrial unconsolidated sands and soils.

881 The measured Poisson's ratio of 0.22 is low compared to values typically assumed for terrestrial
882 sediments. It is close to laboratory data for dry quartz sands: saturated sands show much larger Poisson's
883 ratios, in excess of 0.4, and corresponding v_P/v_S ratios up to and larger than 5 (Ohsaki and Iwasaki, 1973;
884 Prasad et al., 2004). The field experiment on beach sand also yielded a low Poisson's ratio of 0.15
885 independent of depth (Bachrach et al., 2000). The field measurements by Uyanik (2010) resulted in a v_P/v_S
886 ratio of 1.5, corresponding to a Poisson's ratio of 0.1, for the upper tens of cms of dry unconsolidated top-
887 soil, indicating a porous and air-filled environment. These observations demonstrate the strong influence
888 of water content on Poisson's ratio in unconsolidated sands and soils. As no free near-surface water is
889 expected in the regolith at the landing site, but the layer is expected to be porous and to exchange gases
890 with the atmosphere, the low Poisson's ratio and v_P/v_S ratio corresponding to values obtained from the
891 laboratory experiments are plausible first estimates for the InSight landing site.

892 For the Moon, seismic velocities at the surface initially derived from the touchdown of the Surveyor
893 spacecraft yielded very low values of 45 m/s for v_P and 23 m/s for v_S, corresponding to a Poisson's ratio
894 ν of 0.32 (Sutton and Duennebier, 1970). Active seismic experiments of Apollo 14, 16 and 17 found
895 somewhat higher P-wave velocities of the lunar regolith of 100 to 114 m/s in the upper 4 to 12.2 m, with
896 higher velocities in the range of 250 to 330 m/s at greater depth (Kovach and Watkins, 1972; Watkins and
897 Kovach, 1972, 1973; Cooper et al., 1974). The v_P values for the uppermost regolith layer agree well with
898 estimates based on the recordings of the lunar module liftoff with the passive seismic experiments at
899 Apollo 12, 14 and 15, which are in the range of 99 to 103 m/s (Nakamura et al., 1975). Laboratory
900 measurements on lunar soils returned to Earth gave similarly low values for P-wave velocities of 125 m/s
901 at 4 kPa (Johnson et al., 1982). Gangi and Yen (1979) interpreted the data from the Apollo 14 and 16
902 active seismic experiments in terms of a power-law increase of P-wave velocity with depth in the regolith

layer, with an exponent of 1/6 as predicted by contact theory and a velocity of 110 m/s at the surface, which was, however, contested by Watkins and Kovach (1973), claiming that this velocity law does not provide a good fit to the layered Apollo models.

Shear wave arrivals were only tentatively identified in the active recordings of Apollo 14, resulting in an S-wave velocity estimates of 62 m/s and a Poisson's ration ν of 0.23 for the lunar regolith (Kovach and Watkins, 1973), quite similar to the proposed model for the InSight landing site. Additional information has been derived from the passive lunar experiments, e.g., horizontal-to-vertical spectral ratios (H/V) of artificial and natural impacts as well as deeper events (Mark and Sutton, 1975; Horvath et al., 1980). Lunar S-wave velocities were in the range of 32 to 40 m/s at the surface, with values greater than 100 m/s found only below 10 m depth. Resulting Poisson's ratios are 0.41 to 0.43 at the surface, decreasing to 0.33 below. Analysis of Rayleigh waves extracted from ambient noise correlations at the Apollo 17 geophone array yielded S-wave velocity values of 50 m/s for the uppermost 2 m, increasing to 70 m/s at 4 m depth, and a Poisson's ratio around 0.33 (Larose et al., 2005; Sens-Schönfelder and Larose, 2010). A recent re-analysis of horizontal to vertical spectral ratio (H/V) curves in combination with Rayleigh wave dispersion from the active experiments at Apollo 14 and 16 yielded S-velocities of 50 to 60 m/s for the upper 12 to 15 m (Dal Moro, 2015), and Poisson's ratios around 0.33. In contrast, re-analysis of Apollo 17 active seismic data using wavefield gradient analysis resulted in S-wave velocities of 40 m/s for the upper 4 m, underlain by 110 m/s. A Poisson's ratio ν of around 0.41 was indicated in the shallowest layer (Sollberger et al., 2016).

While the low velocities of the lunar regolith are surely due to a high porosity (Tittmann et al., 1972), which also has a profound effect on velocities in terrestrial field experiments (Watkins et al., 1972), the vacuum does not play a major role. In experiments using a granular material consisting of glass beads, Griffiths et al. (2010) observed no difference between seismic velocities measured in vacuum and in ambient air, and only a relatively small decrease of a few percent for vacuum compared with 0.6% interstitial water, even at low confining pressure. In fact, the P-wave velocities for the shallowest layer measured during the Apollo program are in good agreement with terrestrial field measurements on sand and the predictions for the InSight landing site. The velocity law derived by Gangi and Yen (1979) predicts a much smaller increase of velocity with depth compared to the InSight landing site model (Figure 10). To a large extent, the resulting lower velocities at depth can be explained by reduced compaction under the diminished gravity of the Moon, although variations in grain size with depth might also affect the profile (Pilbeam and Vaišnys, 1973). Most measured lunar S-velocities are somewhat lower, and the Poisson's

ratio accordingly higher, than predicted for the InSight landing site and found in dry terrestrial samples. However, the spread in v_S estimates, and correspondingly Poisson's ratio, for the lunar regolith is significantly larger than for v_P, which may explain part of the discrepancy.

4.2. Elastic Modulus

Based on Hooke's law, the elastic or Young's modulus E describes the ratio between uniaxial tensile stress σ and the proportional deformation, or extensional strain, ε, and thus the stiffness of a material:

$$\sigma = E\varepsilon \tag{21}$$

It can be expressed in terms of the shear wave velocity v_s, Poisson's ratio ν and density ρ as

$$E = 2v_S^2\rho(1 + \nu) \tag{22}$$

Depth profiles of Young's modulus for the three different models of regolith compaction are given in Figure 3. The values are lower than those obtained for some field tests on terrestrial soil, that found E increasing from 30 to 90 MPa in the upper 0.6 m (Uyanik, 2010), and on sand, that deduced E between 20 to 70 MPa in the uppermost meter (Jaksa et al., 2004). In their overview, Bowles (1966) quote values between 5 and 25 MPa for E in silty to loose sand and a range of 50 to 81 MPa for dense sands, though, in good agreement with values calculated here. Teanby et al. (2016) also obtained low values for the effective E in the range of 1.1 to 4.4 MPa when applying elastic theory at two sites located on very loose basaltic sands in Iceland. These values are likely appropriate only for the uppermost few centimeters of the subsurface, whereas the profiles in Figure 11 show slightly larger values around 7.5 MPa.

In situ measurements of Young's modulus for the Moon were not reported but Alshibli and Hasan (2009) determined E by laboratory experiments for the JSC-1A lunar regolith simulant, which is mined from a volcanic ash deposit in a commercial quarry. They measured values in the ranges of 11.1 to 15.5 MPa and 10.3 to 27.6 MPa for loose and dense packing, respectively, at pressures corresponding to 2 and 4 m depth on Mars (10 and 20 kPa). These values are considerable lower than the values for E calculated here, but JCS-1A has a large proportion of small grains, with more than 55% of grains smaller than 100 µm. Thus, JSC-1A is not a good analogue of the regolith at the InSight landing site.

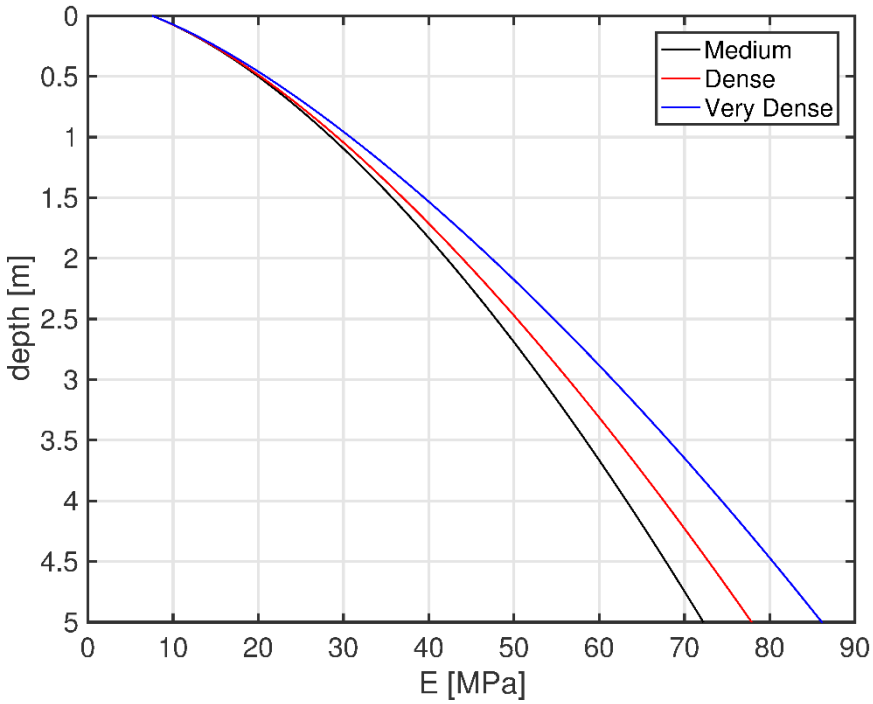

Figure 11: Models of Young's modulus as a function of depth for the upper five meters of regolith at the InSight landing site. The three profiles correspond to the density profiles shown in Figure 3 based on different states of regolith compaction.

957

958 ## 4.3. Attenuation Factor

959 Seismic attenuation is the dissipation of energy through internal friction and other non-elastic
960 processes and affects the amplitude of seismic signals propagating through natural materials. Attenuation
961 is quantified by the dimensionless seismic quality factor Q, defined via the decrease of amplitude A at
962 frequency f after travelling a distance x through a medium with seismic velocity v

$$A(x) = A_0 e^{-\left(\frac{f\pi}{Qv}\right)x} \tag{23}$$

963 (Lay and Wallace, 1995). Note that this equation defines attenuation caused by intrinsic anelasticity and
964 does not include apparent attenuation due to scattering, i.e., the redistribution of energy to the coda of
965 a seismic phase due to small-scale heterogeneity along the wave path. For the Moon, attenuation due to
966 intrinsic anelasticity is much lower than on Earth, while scattering in the lunar crust is much larger, which,
967 in combination, result in the characteristic signal shapes of lunar seismograms (e.g., Dainty and Toksöz,

968 1981). The envelope of these seismograms can be fairly well modeled by diffusion theory (see Lognonné
969 et al., 2009; Gillet et al., 2017; for recent applications). No laboratory measurements of Q are available
970 for Martian regolith analogues. Thus, the discussion is focused on available theories and on data from the
971 Moon and Earth, which are clearly different, and what can be deduced from these for Mars.

972 S-wave quality factors Q_S, obtained by borehole measurements in terrestrial sediments and soils, lie
973 between 3 and 35 (e.g., Gibbs et al., 1994; Assimaki et al., 2008; Parolai et al., 2010; Fukushima et al.,
974 2016). From surface measurements on Quaternary sediments, Malagnini (1996) determined a frequency
975 dependence in Q for both P- and S-waves, with $Q_P = Q_S = 9$ at 10 Hz, compared to a value of 2 previously
976 found at 1 Hz (Malagnini et al., 1995). Frequency dependence in Q at frequencies of a few Hz is generally
977 attributed to the influence of scattering (e.g., Kinoshita, 2008), which we do not consider further here.
978 Jongmans (1990) found similarly low values, on the order of 5, for Q_P in field measurements on
979 unsaturated sand. Laboratory measurements on dry quartz sands showed Q_S in the range of 15 to 50 at
980 lowest confining pressures below 0.3 MPa and Q_P around 10 to 15 (Prasad and Meissner, 1992).

981 In contrast to terrestrial data, Apollo experiments determined unusually high Q values in the lunar
982 interior, ranging from 3000 to 3600 in the upper crust (Latham et al., 1970a, b) to 4000 to 4800 in the
983 upper mantle for both P- and S-waves (Nakamura et al., 1976; Nakamura and Koyama, 1982). These high
984 Q values also extended up to the near-surface material, including the lunar regolith and the somewhat
985 faster layer below, for which Nakamura (1976) determined 2000 as a lower limit for Q from interpretation
986 of rover signals. Analysis of the Apollo 14 seismic experiment data gave an estimate of 50-100 for Q of
987 the near-surface lunar material (Kovach and Watkins, 1972). Recently, Dal Moro (2015) found that high
988 Q_S values of at least 100 in the uppermost regolith and 300 below the slowest layer to a few 100 m depth
989 in the shallow crust are essential in obtaining a good fit to measured H/V curve amplitudes. As these data
990 cannot differentiate further between Q_S values of either a few hundred or significantly larger ($\geq$ 1000),
991 they are not in conflict with previous higher estimates which averaged over larger depth ranges.

992 As demonstrated in laboratory experiments, high Q values are caused by extremely low water content
993 in the rocks from which even thin layers of adsorbed water have been removed by strong outgassing
994 under vacuum conditions (Tittmann, 1977; Schreiber, 1977; Tittmann et al., 1979). As discussed by
995 Tittmann et al. (1972), laboratory measurement of Q factors on returned lunar samples failed to
996 reproduce the high values measured in situ on the Moon when exposing the samples to laboratory air
997 during the measurements, and values around 50 to 100 were obtained. Only by outgassing the samples

998 under high vacuum, could Q values of 3000 to 4500 be achieved, in agreement with the in situ estimates
999 for lunar rocks. However, Q returned to the low original values after a few minutes re-exposure to
1000 laboratory air (Tittmann et al., 1979). However, all of these measurements pertain to lunar rocks, not
1001 fines. A similar observation was reported by Pandit and Tozer (1970) for porous terrestrial rocks, with an
1002 increase in Q by a factor of 5 between terrestrial atmospheric pressure and 1.5 Pa. Tittmann et al. (1980),
1003 working with porous sandstone, showed that the first monolayer of adsorbed water has the strongest
1004 effect and decreases Q by a factor of about 5 compared to the vacuum-dry case. In the Martian crust an
1005 evacuation of trapped fluids comparable to the lunar situation is prevented by atmospheric pressure, as
1006 it requires successive heating cycles at pressures below 1.5 Pa (Lognonné and Mosser, 1993). Accordingly,
1007 Q is predicted to be larger by at most a factor of two compared to Earth for Martian crustal rocks.

1008 A laboratory experiment on fines was conducted by Jones (1972). Jones used powdered basalt with a
1009 mean particle diameter of 5 μm and a mean density of 1340 kg/m^3, significantly finer than the sand at the
1010 InSight landing site, but with a similar surface density to that estimated here. At 10 Hz Jones found a clear
1011 increase in Q with decreasing pressure, from values of Q_P around 50 at ambient conditions to 100 at Mars
1012 surface atmospheric pressure, to 120 at about 5 Pa. Jones inferred that remnants of lubricating water
1013 films are still present at these pressures as compared to measurements made in a vacuum. For glass
1014 beads, 400-800 μm in diameter, Griffiths et al. (2010) reported differences in Q by a factor of 4.5 between
1015 200 in ambient air with about 25% humidity, and 900 in a vacuum. Brunet et al. (2008) obtained a Q of
1016 295 for a similar granular material of glass beads, 600-800 μm in diameter, dried in a furnace, and
1017 measured under ambient conditions. According to contact theory for spherical particles, certain variables,
1018 including Q, are proportional to particle radius (Brunet et al., 2008), which could explain the different
1019 values obtained for Q in the different experiments.

1020 Laboratory measurements on dry quartz sand yield Q_P/Q_S ratios ranging from 0.2 to 1.8 (Prasad and
1021 Meissner, 1992; Prasad et al., 2004). Studies on porous sandstones yield equal values for Q_P and Q_S at
1022 low confining pressures when performing measurements under ambient laboratory conditions and after
1023 drying the samples in a laboratory oven (Toksöz and Johnson, 1979). Based on the limited information
1024 available, we assume that Q_P and Q_S are approximately equal at the InSight landing site.

1025 One of the main factors controlling Q is the regolith water content. Laboratory measurements have
1026 shown that a single monolayer of adsorbed water can drastically reduce the high Q values observed in
1027 outgassed lunar or terrestrial samples (Tittmann et al., 1979, 1980). Pandit and Tozer (1970) reported

that the large change in Q they observed was connected to a change in water content of less than 0.05 wt.%. Any liquid or frozen surface water would not be in equilibrium in the equatorial regions of Mars targeted by the InSight lander and would quickly sublimate (Golombek et al., 2017). However, water within the regolith could still be present in the form of a few monolayers of adsorbed water (Möhlmann, 2008), which would maintain liquid-like properties down to temperatures of −70°C (Lorek and Wagner, 2013). This adsorbed water is supposed to reside mainly below depths of a few tens of cm, outside the range of the Martian diurnal and seasonal thermal cycles (Möhlmann, 2004). Such a two-layered regolith structure would be consistent with a model for regolith water content derived from neutron spectroscopy data (Feldman et al., 2004), which assumes a relatively desiccated near surface layer with 2 wt.% water and a more water-rich layer below, with at least 6 wt.% water. Furthermore, given that the Martian regolith is expected to be in exchange with the atmosphere (see Section 6 below), it seems reasonable to assume that monolayers of water could be present, but the amount of water in the regolith depends on latitude and season (Martinez et al., 2017). This would also be consistent with degassing experiments performed by the SAM (Sample Analysis on Mars) instrument suite on the Curiosity rover at Gale crater (Leshin et al., 2013), which found loosely bound water degassing from the samples starting at around 100°C.

Therefore, we provide models for Q values for the Martian regolith that are based on Mindlin theory (Figure 12), as used by Brunet et al. (2008) to interpret their data from measurements with dry beads. The resulting values are consistent with results obtained in lab experiments on basalt fines and granular materials in dry, but non-vacuum conditions, taking into account estimates for regolith particle size. The theory predicts a dependence of Q on pressure with an exponent of 2/3, which is within the observed range of 0.5 to 0.9 for spherical grains (Pilbeam and Vaišnys, 1973). Observations for angular grains found a smaller pressure dependence with an exponent of 0.3 to 0.4 (Pilbeam and Vaišnys, 1973). The increase of Q with depth could thus be lower if the particle grains at the landing site are less than perfectly spherical. In addition, Q also depends on particle size. We used a particle radius of 100 µm, in the center of the range for fine sand when calculating the curves in Figure 12. However, a non-uniform particle size will result in deviation in the predicted values for Q. Specifically, if particle size increases in the upper 5 m of the regolith, the increase in Q with depth will be larger. Finally, Mindlin theory also predicts an inverse dependence of Q on displacement amplitude which was not observed in some low pressure experiments (Pilbeam and Vaišnys, 1973). Here we consider amplitudes related to the low end-member strain analyzed by Brunet et al. (2008), on the order of 5×10^{-6}, to avoid decreasing Q.

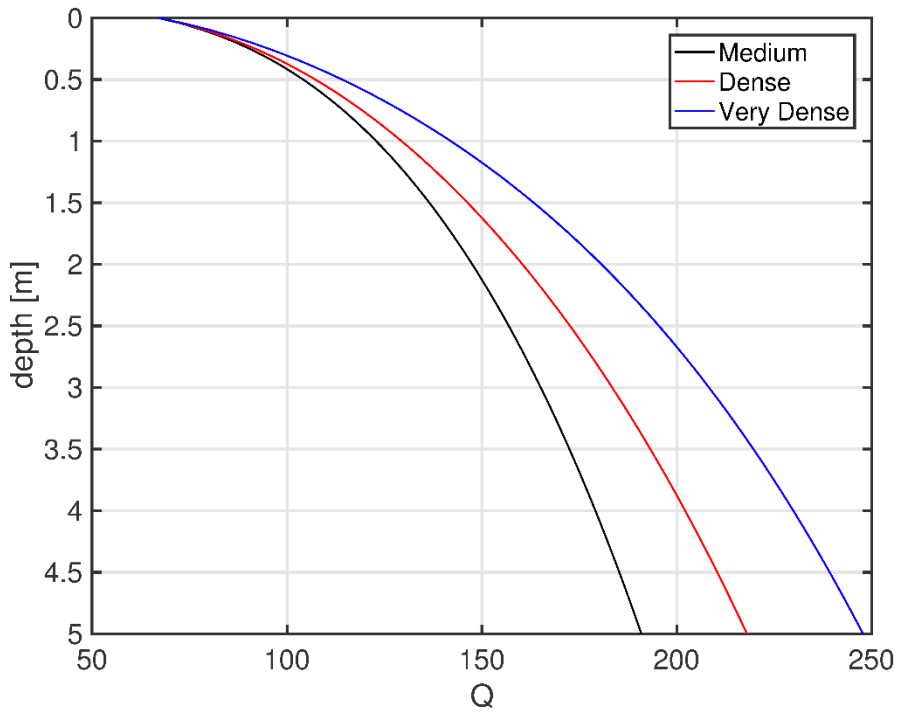

Figure 12: Models of *Q* as a function of depth for the upper five meters of regolith at the InSight landing site. The three profiles correspond to the density profiles shown in Figure 3 based on different states of regolith compaction.

The Q values estimated here are lower than some of the estimates for the lunar regolith, but distinctly higher than terrestrial values. However, it is worth repeating that if no adsorbed water is present in the Martian regolith, Both Q_P and Q_S could be larger than the values given here by up to an order of magnitude.

Surface waves have their amplitude maximum at one-third of their wavelengths. Thus, short period surface waves with a period of 7 Hz, such as those observed in autocorrelations of Apollo 17 geophone data from the Moon, and a group velocity of about 100 m/s based on the estimates in Section 5.1, are strongly influenced by the regolith layer. The range of Q deduced here would indicate approximately 5 to 6 s of propagation time for one Q cycle, or 500 to 600 m of propagation distance for these waves. Amplitude could be reduced by a factor of two after 500 to 600 m of propagation, limiting the observational range of the waves.

5. Mass Diffusivity

The section concerns the *mass diffusivity*, or *coefficient of mass diffusion*, of the Mars atmosphere with respect to the porous medium of the regolith at the InSight landing site. This parameter is important because the atmosphere flows in and out of the regolith in response to changes in atmospheric pressure, and has the potential to convectively transfer heat in and out of the regolith. Convective heat transport associated with atmospheric pressure changes could be indicated by transients in the HP^3 temperature data and/or variations in calculated heat flow with depth. Mass diffusivity is somewhat analogous to thermal diffusivity where thermal diffusivity can be used to describe heat diffusion in the subsurface (see subsection 4.6 Thermal Diffusivity above). In a simplified form, effective mass diffusivity, D_{eff}, may be defined by the following equation (*cf.*, Scanlon et al., 2002, equation 8.31):

$$\frac{\partial M}{\partial t} = D_{eff} \frac{\partial^2 PM}{\partial z^2} \tag{24}$$

where M is mass of the diffusing gas, t is time, and z is depth. Unlike heat flow, however, in porous media the gas molecules flow through the pores rather than through the minerals grains (heat may also be transferred through pores by radiation). Gas molecules have random motion, influenced by pressure gradients, and their interactions with the minerals depend on the molecular gas mean free path, λ, relative to the average pore radius, r.

Mass diffusivity has been measured in terrestrial regoliths (soils and subsoils) under the same conditions of atmospheric pressure change as we are interested in Mars. Cyclic changes in atmospheric pressure that propagate into the subsurface are commonly known as *barometric pumping* or *atmospheric breathing*. On Earth they are of interest in studies of gas exchange associated with plant growth in the vadose zone and in studies of vertical transport of contaminated gases in the porous subsurface (*e.g.*, Nilson et al., 1991; Massmann and Farrier, 1992; Rossabi and Falta, 2002; Massmann, 2006; Rossabi, 2006). These studies are applicable to barometric pumping on Mars at the macro scale, *i.e.*, in the pumping theory, but miss an important difference in the pressure diffusivity at the molecular scale between Earth and Mars. As a consequence of Mars' low atmospheric pressure, molecules in the regolith of Mars have a much higher mean free path than molecules in the terrestrial regolith. They interact more with the pore walls than with their neighboring gas molecules, whereas terrestrial gas molecules generally interact more with each other except in very fine-grained materials, such as shales. Terrestrial gas molecules in porous media interact with the pore walls when the pores are very small. Pore-wall

interactions are important in terms of the permeability and pressure diffusivity of the Mars regolith, and are discussed below. There is one set of experimental measurements of pressure diffusivity under Mars surface atmospheric conditions (Fanale et al., 1982a): these results are discussed and compared with theoretical calculations after presentation of molecular gas interactions in porous media.

5.1. Gas Interactions in Porous Media

At low mass concentrations and in small pore passages, diffusion of gas molecules in porous media involves collisions between the gas molecules and the porous media in addition to molecular interactions among the gas molecules. Mass diffusivity and permeability are both parameters that relate to the flow of fluids through porous media, but they are not simply related because mass diffusivity includes the effects of compressibility, especially when the fluid is a gas (*e.g.,* Liang et al., 2001). However, some of the interactions among gas molecules with pore walls that apply to mass diffusivity were first studied and observed in permeability. One of the interactions of gas molecules with pore walls is slip of gas molecules near a solid wall. Klinkenberg (1941) first addressed how this interaction can affect the measured permeability of a gas, and he proposed a linear permeability correction. Four modes of diffusion have been described which are usually distinguished by the Knudsen number, K_n (*e.g.*, Ziarani and Aguilera, 2012):

$$K_n = \frac{\lambda}{\delta} \tag{25}$$

where λ is mean free path of the gas molecules and δ is a characteristic length, such as the pore diameter. Three of the four modes of diffusion are illustrated in Figure 13 and the four modes and their relations to the Knudsen number are described in Table 3.

For small Knudsen numbers that are applicable to most terrestrial gas flows in natural porous media, pressure diffusivity coefficients representative of Darcy flow are appropriate. However, as the Knudsen number increases to where slip flow on pore boundaries dominates, a new diffusion coefficient, the Knudsen diffusivity, is more accurate (see Table 3). The Knudsen diffusion coefficient, D_k, is given by (*e.g.*, Huizenga and Smith, 1986; *Roy* et al., 2003; Javadpour et al., 2007):

$$D_k = \frac{\delta_p}{3}\sqrt{\frac{8RT}{\pi M}} \tag{26}$$

where δ_p is the pore diameter R is the universal gas constant, T is absolute temperature, and M is the gas molar mass. Under conditions of Knudsen diffusion (Table 3, $K_n > 10$), D_k is the appropriate diffusion coefficient to use in Equation 24 in place of D_{eff}.

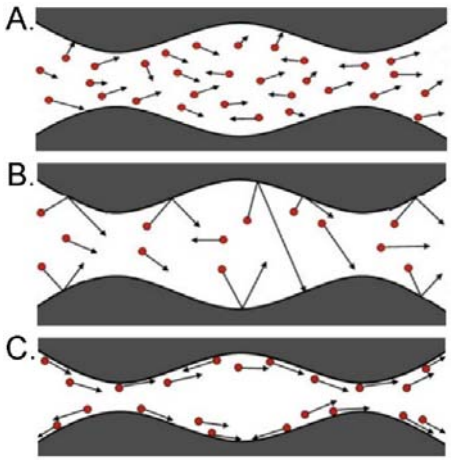

Figure 13: Diagrammatic cross-sections of pores and gas molecules with a small pressure gradient from left to right, illustrating different modes of diffusion flow: A. molecular or bulk diffusion; B. Knudsen diffusion; and C. surface diffusion. Different modes of diffusion are illustrated separately here for clarity, but in nature two or more modes may co-exist (diagram modified from Ziarani and Aguilera, 2012, Figure 1).

Table 3: Knudsen number and flow regimes classification for porous media (after Karniadakis et al., 2005). Calculations indicate that atmospheric flow in the regolith at the landing site is in the Transition flow regime ($0.1 < K_n < 10$).

Flow Regime	Knudsen Number	Model Applied	Comment
Continuum (viscous) flow[1]	$K_n < 0.01$	Darcy's equation for laminar flow; Forchheimer's equation[2] for turbulent flow.	Assumes immobile fluid at pore wall. Hence, no permeability correction generally required.
Slip flow	$0.01 < K_n < 0.1$	Darcy's equation with Klinkenberg or Knudsen's correction.	Knudsen's equation more accurate, but Klinkenberg correction easier.
Transition flow	$0.1 < K_n < 10$	Darcy's equation with Knudsen's correction or Burnett's equation with slip boundary conditions[3].	Knudsen's diffusion equation more reliable, especially when K_n close to 10.
Knudsen's (free molecular) flow	$K_n > 10$	Knudsen's diffusion equation[4]; alternative methods are DSMC and Lattice Boltzmann methods[3].	Usually applies to shale where pore-throat radii are very small.

[1] Some references suggest $K_n < 0.001$ as a limit for continuum flow (*e.g.*, Roy et al., 2003);
[2] *e.g.*, Whitaker (1996);
[3] For more detail see Agarwal et al. (2001). DSMC = Direct Simulation of Monte Carlo;
[4] Knudsen diffusion can coexist with bulk and surface diffusion

5.2.Estimating Pore Sizes

Many variables contribute to the pore radii in sediments and porous rocks, including grain size, degree of sorting, compaction, cementation, moisture content, diagenesis, and growth of secondary minerals. There is evidence of wind and water processes on the surface of Mars, both of which would tend to sort and round grains in the regolith. Impact processes produce angular fragments and poorly sorted materials. The landing ellipse for the InSight landing site was chosen to be on smooth, flat terrain that generally has a very low rock abundance and as few impact craters visible in high-resolution orbital images as possible (Golombek et al., 2017). Selection criteria for the landing site in the northern lowlands and with a paucity of impact craters should make impact fragmentation subordinate to abrasion as a mechanical weathering process at the landing site. The particles in the landing site regolith may therefore be expected to be well-sorted, rounded grains, as described in Section 2 above.

Although relations have been proposed, no universal simple relation exists in sediments between grain size and pore radii from which the pore radii may be estimated. Kaviany (1994) proposed a relation among average pore size, particle diameter and porosity for spherical particles in random packing. If a fractional porosity of 0.399 is assumed, representative of random packing of uniform spheres, this relation gives a ratio of average pore size to grain size, δ_p/d_g, of 0.072, where δ_p is pore size and d_g is the grain diameter. Minimum pore throat diameters were calculated geometrically assuming the most inefficient regular packing of uniform spheres (Cubic packing, 0.476 porosity), and the most efficient regular packing of uniform spheres (Triclinic, or hexagonal close packing, 0.260 porosity). For cubic packing the minimum throat diameter is given by $0.207d_p$ (δ_p/d_g = 0.21); for triclinic packing the minimum throat diameter is given by $0.0774d_p$ (δ_p/d_g = 0.077). Assuming a porosity representative of random packing, the ratios of pore diameter or pore throat diameter to grain size (δ_p/d_g) calculated from the from the Kaviany (1994) equation are very similar to those calculated geometrically for triclinic (close-hexagonal) packing, 0.072 versus 0.077, respectively. Cubic packing is improbable in sorted spherical grains as they are unlikely to be balanced in vertical columns.

One further complication in determining pore size from grain size is that the methods discussed above all assume uniform spherical grains, a condition that may not exist in the Mars regolith. Variations in grain size and deviations from spherical shape are both likely to reduce pore size as smaller grains would fill larger pore spaces and flattening of the grains would result in compaction: reduced pore size would reduce pressure diffusivity. However, at the InSight landing site the surface regolith sediment is likely to

be well-sorted and rounded from eolian processes. Using the estimated range of grain size of 0.125 to 0.25 mm (radii 0.0625 to 0.125 mm) from Subsection 2.1 Landing Site Overview above, and an average δ_p/d_g ratio of 0.075, a range of pore throat diameters of 9.4 to 18.8 µm was calculated. At the InSight landing site these pores would be subject to an atmospheric pressure range of 6 to 8.5 hPa.

5.3. Gas Mean Free Path and Range at Landing Site

The mean free path of molecules in a gas is estimated by considering the volume of a cylinder that represents the gas molecules effective collision area, including the area of target molecules in this area, with respect to the distance travelled by the molecules and the number of molecules per unit volume (*e.g.*, Nave, 2016). The number of molecules per unit volume of gas may be approximated by assuming that the systems behaves as an ideal gas (Tan, 2014). The calculation must also recognize that both the colliding and the target molecules are moving (Nave, op. cit.). These assumptions yield the result that the molecular mean free path, λ, may be estimated by:

$$\lambda = \frac{RT}{\sqrt{2}\pi\gamma^2 N_a P} \tag{27}$$

where R is the universal gas constant, T is absolute temperature, γ is the effective collisional diameter of the molecules, N_a is the Avogadro number, and P is pressure. The effective collisional diameter of CO_2 is 330 pm (*e.g.*, Albrecht et al., 2003), and at a temperature of 180 K and pressures of 6 and 8.5 hPa, molecular mean free paths of 8.56 and 6.04 µm were calculated for CO_2. At a temperature of 270 K and pressures of 6 and 8.5 hPa, molecular mean free paths of 12.8 and 9.06 µm were calculated. This array of conditions and calculated molecular mean free paths should cover the range of likely diffusivity environments to be encountered at the InSight landing site.

5.4. Calculated Range of Mass Diffusivity at Landing Site

Knudsen numbers were calculated using the molecular mean free paths calculated with equation 27 for the range of pore diameters estimated above, and corresponding Knudsen diffusion coefficients were calculated using equation 27. These results indicate that gas flow in the shallow regolith at the InSight landing site will probably be in the Knudsen Transition Flow range with Knudsen diffusivities ranging from of 1 to 2 x 10^{-3} m^2/s. To give a direct comparison of Knudsen diffusivity with grain size when in the pore and pressure range for which the Knudsen diffusivity equation is applicable, Knudsen diffusivity is plotted

as a function of grain size in Figure 14 for the expected range of grain sizes for the near-surface regolith at the InSight landing site.

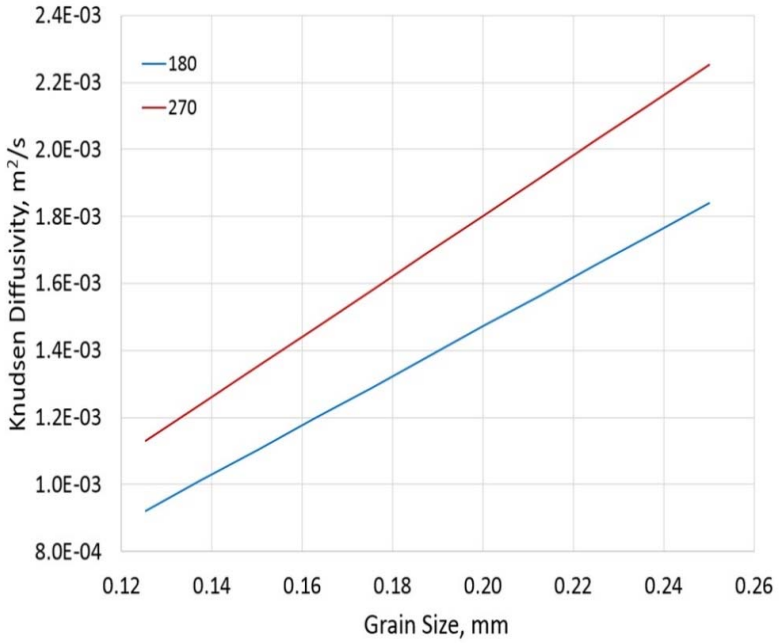

Figure 14: Knudsen Diffusivity (Pressure diffusion coefficient) versus regolith grain size for regolith and atmospheric conditions likely to occur at the InSight landing site. The numbers given by the key to the curves are temperature in Kelvin.

5.5.Comparison with Experimental Data

Fanale et al. (1982a) built an experimental system to determine the mass diffusivity of a *Mars simulant soil* (45% smectite, 45% finely-ground basalt, and 10% iron oxide) with a density of 1300 kg/m^3 at temperatures of -40^{o}C (233 K) and -70^{o}C (203 K). Diffusivity was determined by measuring the rate of penetration of a CO_2 pressure wave with a starting pressure of ~6 hPa and a pressure step of ~2 hPa. The experimentally estimated diffusivities were 2.5 x 10^{-6} and 1 x 10^{-6} m^2/s for temperatures of 233 and 203K, respectively. Fanale et al. (1982a) did not give an estimate of the average pore diameter of their Mars simulant soil, but presumably the pores were very small as 90% of the simulant was smectite and finely-ground basalt. Their determined diffusivity range is three orders of magnitude smaller than the diffusivities calculated above. The primary difference in the diffusivities determined experimentally and the diffusivities calculated here may be explained by the smaller pore sizes in the experimental regolith simulant.

An additional phenomenon, discussed by Fanale et al. (1982b), is the adsorption of CO_2 onto the grains of the regolith. The adsorption of gases, including CO_2, onto the surface of clays had been previously reported (*e.g.*, Aylmore et al., 1970; Fanale and Cannon, 1979). The adsorption of molecules onto grain surface tends to decrease pore diameters but does not reduce slip flow as molecules can slip over molecules adsorbed onto grains. CO_2 molecules are less than 0.001 µm in their longest dimension which much smaller than the pore sizes discussed above (9.4 to 18.8 µm). Thus, even if several layers of CO_2 molecules adhere to the pore walls the reduction in pore size would be small. The effect would be to increase the Knudsen number, but it would be unlikely to move out of the transition flow mode, with a small accompanying decrease in mass diffusivity. These effects are likely to be very minor: a 0.01µm (10-20 layers of CO_2 molecules) reduction in the minimum pore size (9.4 µm) would result in a 0.11% increase in the Knudsen number and a 0.11% reduction in the Knudsen diffusivity. Adsorption of CO2 could also impact the mass diffusivity by acting as a temporary reservoir for CO2, storing CO2 by adsorption during pressure increases and releasing the adsorbed CO2 during pressure decreases. This effect could result in a hysteresis in atmospheric breathing that could be complicated by the temperature sensitivity of adsorption.

5.6. Final Observations

Mass diffusivity is an important parameter to the InSight mission because it constrains the flow of the Mars atmosphere into and out of the regolith at the landing site in response to changes in atmospheric pressure. This is a well-known phenomenon on Earth. Although the pumping process is similar on Mars to Earth, the molecular processes controlling mass diffusivity are different as a consequence of the low pressure of the Mars atmosphere: on Earth gas molecular collisions are dominantly with neighboring gas molecules; on Mars gas molecular interactions are dominantly with regolith grain surfaces. Using a calculated range of pore sizes based on the assumption of uniform-size, spherical grains at the landing site, a range of mass diffusivities of 1 to 2 x 10^{-3} m^2/s was calculated. This is probably a high estimate as grains of variable size and non-spherical grains would generally result in smaller pores than uniform-size spherical grains. The calculated diffusivity range based on simplified grain geometry is significantly higher than an experimentally determined range of mass diffusivities for the Mars regolith of 1 x 10^{-6} to 2.5 x 10^{-6} m^2/s (Fanale et al., 1982a). A probably explanation for the difference between the calculated and experimentally determined diffusivity ranges is that the regolith simulant used by Fanale et al. (1982a) in their diffusivity determination was very fine grained. The inclusion of 45% smectite, a clay, in their sample suggests that at least part of their sample had a grain size in the range of ~0.1 to 0.4 µm. Assuming the

same pore size to grain size as used above, a range of Knudsen numbers equivalent to the curves in Figure 14 of 20 to 43 was calculated corresponding to Knudsen diffusivity range of 1.0 to 2.6 x 10^{-5} m^2/s for 203 K and 1.1 to 2.6 x 10^{-5} m^2/s for 233 K. These results are about an order of magnitude lower than the diffusivities estimated experimentally, the differences probably being caused by the assumption of uniform spherical grains in the pore size approximation for the calculations: clays have platy grains and the average pore sizes in the experimental mixture were likely to be smaller than assumed here resulting in a lower experimental diffusivity. However, a grain size range of 0.125 to 0.25 mm and the calculated effective mass diffusivity with this grain-size range is thought to be more representative of the InSight landing site.

What are the implications of the calculated mass diffusivities for the penetration of periodic atmospheric pressure waves into the regolith at the landing site? If we make the assumption that the regolith is homogeneous and isotropic, a penetration skin depth δ can be calculated as $\delta = \sqrt{(2\pi D_{eff}/\omega)}$, where ω is the angular frequency of the period wave. The skin depth is the depth at which the maximum amplitude of the pressure change is 1/e (~ 37%) of the maximum surface pressure change. For a wave with a period of 1 sol (24 hours 40 min), δ = 9.4 m for D_{eff} = 1.0 x 10^{-3} m^2/s, and δ = 13.2 m for D_{eff} = 2.0 x 10^{-3} m^2/s. For a wave with a period of Mars year (687 days), δ = 244 m for D_{eff} = 1.0 x 10^{-3} m^2/s, and δ = 345 m for D_{eff} = 2.0 x 10^{-3} m^2/s. These are large depths relative to the maximum penetration of the HP^3 probe of 5 m. The time for a diffusive disturbance to travel a characteristic length L_c of 5 m is about 0.29 sol for a diffusivity of 1.0 x 10^{-3} m^2/s, and about 0.14 sol for a diffusivity of 2.0 x 10^{-3} m^2/s (using the approximation $L_c^2 = D_{eff}\, t$, where t is time). However, the effect of flow of atmospheric gases in and out of the regolith in terms of heat transport and the HP^3 heat-flow determination depends on the relative efficiencies of convective gas heat transport and conductive heat transport (possibly aided by intergranular radiative heat transport. This problem has been examined by Morgan et al. (2017). Their highest estimate of mass diffusivity was an order of magnitude lower than we have concluded here for the regolith at the InSight landing site, but they concluded that the diffusivity would need to be higher by a factor of about 100 for convection to be more efficient than conduction with reasonable estimates of the thermal conductivity of the regolith. This conclusion is based on several estimated parameters, but current information indicates that atmospheric gases will be forced into the regolith by changes in atmospheric pressure, but thermal convection by these movements will be insignificant.

6. Summary and Conclusions

There were a number of primary engineering criteria for the InSight landing site which to some extent affected the physical properties of the landing site. These criteria included latitude (equatorial for solar power), low elevation (avoid cold temperatures), smooth plains with few rocks and craters (safe landing site), and fragmented regolith (to be penetrated by the self-hammering, heat-flow probe – HP^3). These criteria resulted in the selection of a 130 x 27 km landing ellipse at 4.5°N, 135.9°E in western Elysium Planitia on Hesperian plains in the southernmost lowlands.

Thermophysical properties used in the site-selection process indicated a regolith at this site similar to weakly-bonded terrestrial soils, capable of being penetrated by the HP^3 probe. The properties indicated that the soil was cohesionless sand or low cohesion soil with a bulk density of ~1,000 to 1,600 km m^{-3} and grain sizes of ~0.15 -0.25 mm (fine sand). A cover of surficial dust was indicated, less than 1-2 mm thick, and with low rock abundance. The upper 5 m of the regolith were predicted to be composed of nearly cohesionless, fine, well-sorted, rounded to sub-rounded, basaltic sand, which included few rocks.

Based on studies of terrestrial soils and from heat-flow observations on the Moon, the regolith density is likely to significantly increase with depth as a result of compaction. The lunar heat-flow results required a rapid increase in thermal conductivity associated with compaction with depth. Compaction caused by gravity and impacts have resulted in models based on lunar compaction but the models are uncalibrated for Mars.

Information covering cohesion of the Mars Regolith at the InSight landing site has been compiled from mechanical arms from Mars landers and the wheels of rovers. Cohesions range from cohesionless to weakly cohesive soils, less than 4 kPa, with blocky soils having higher cohesions of 3-11 kPa. The landing site will probably have a thin layer of cohesionless to weakly cohesive eolian deposits at the surface. These deposits may be blown away by the pulsed jets of the lander, below which the regolith will be weakly cohesive.

Internal friction angle is sensitive to factors including material grain shape and bulk density. Many Mars regolith simulants have had angular grains that are probably not representative of the rounded to sub-rounded grains subject to wind erosion at the landing site. Extrapolation of experiments with rounded grains and a bulk density of 1,300 km/m^3 have provided a friction angle of 28° to 30° for the

landing site. If the assumption is made that particle shape does not change with depth, internal friction angle may be predicted as a function of bulk density and depth.

Grain size is an important factor in many physical properties and is primarily constrained to be in the range of 150-250 µm (fine sand) by the thermal inertia of the landing site. Theoretical studies and observations at the Phoenix landing site in the Martian Arctic indicate that there is a transition below 600 µm from larger clasts to the dominant fine sand grain size. Finer material may be found in this surficial dust layer.

At this stage, thermophsyics properties have been assumed to change only with depth. Measurements of surface emissivity on Mars has been from satellite sensors and from a sensor on the Mars Science Laboratory rover. These data have allowed weighted average emissivities to be derived for the three wavelength bands corresponding to the HP^3 radiometer filters at 235 K for four different types of soils measured *in situ* by the Mars Exploration Rovers' mini-thermal emission spectrometer instruments.

Surface thermal inertia controls the rate of change in temperature of the upper 2-30 cm of the regolith, and is strongly related to the square root of thermal conductivity. The lowest thermal inertias in the landing region are typically observed where atmospheric dust and very fine sand are trapped; the highest thermal inertias are associated with coarse regolith on crater rims and ejecta blankets.

Surface albedo from different areas of Mars has been measured at different resolutions from orbiting satellite systems. Landers with retropropulsive thrusters have changed the surface albedo by temporarily removing the surface dust layer at all landing sites where the thrusters have been used. A temporary albedo reduction of ~20-50% at the InSight landing site during landing is anticipated.

Based on in situ determinations of the thermal conductivity of the lunar regolith during two of the Apollo missions, and a number of published experiments simulating lunar and Mars regolith conditions, the thermal conductivity of the shallow regolith at the landing site is anticipated to be of the order of 0.01 W/(m K), about two orders of magnitude lower than the thermal conductivity of damp terrestrial soils. As bulk density changes with depth, thermal conductivity is anticipated to change with depth. In addition, although atmospheric pressure is much lower, the fractional changes in atmospheric pressure during the diurnal and annual cycles are much greater on Mars than on Earth. As heat transfer through the gas in pore spaces is significant on Mars, the bulk thermal conductivity is sensitive to changes in atmospheric pressure.

Studies of the heat capacity (units J/K) or specific heat (units J/(kg K)) of lunar, geologic, and meteorite materials at low temperatures indicate that these parameters are strongly temperature dependent, increasing with increasing temperature. This temperature dependence is most significant in the near-surface regolith layer where there are large temperature perturbations associated with diurnal and annual temperature variations. Below a few tens of cm these perturbations decay and an average heat capacity/specific heat may be used.

Thermal diffusivity is the parameter in thermal conduction associated with the propagation of temperature changes, such as transmission of the annual temperature variation into the regolith. As with other thermal parameters, it is probably most variable in the upper few tens of cm of the regolith at the landing site, and is fairly constant below this depth.

Subsurface elastic properties are of particular importance to the data to be collected by the seismometer experiment (SEIS) when operating at its highest rate and for short period surface waves above 5 Hz. There are no remote sensing data or existing lander results from which these properties may be derived and thus at present they are estimated from laboratory measurements. Seismic body wave measurements indicate that seismic velocities are very slow within the regolith but a significant increase in velocities may be expected between the surface and 5 m depth. In contrast, experiments on Mars regolith simulants and similar materials indicate that Poisson's ratio will be relatively constant with depth in dry, shallow regolith, but lower than most estimates for the Moon or measured in water-saturated terrestrial soils. Young's Modulus increases rapidly with depth, similar to the body-wave velocities. Seismic attenuation (dissipation of seismic energy by non-elastic processes), as measured by the seismic quality factor, Q, is expected to be relatively high in the Mars regolith, but depends to a large extent on the presence of adsorbed water, a parameter for which there are no direct observations at the InSight landing site. Q was measured to be very high, both in the regolith and at depth, on the Moon relative to terrestrial values, reflecting the very dry state of the Moon. A very small amount of water, monolayers in thickness, on the grains in the Mars regolith could be sufficient to significantly reduce Q by an order of magnitude, however. If no water is present Q would be close to lunar values.

Mass diffusivity of the landing site regolith is the parameter that relates the flow of the Mars atmosphere in and out of the regolith in response to changes in surface atmospheric pressure. Most landing site physical parameters change from Earth to the Mars regolith because of differences in water saturation, atmospheric pressure, compaction, composition, etc. Mass diffusivity changes from Earth to

Mars, except in a few special terrestrial examples, in that the mode of gas transport is dominated by molecule-grain collisions in the landing site regolith and a mass diffusivity equation appropriate to this mode (Knudsen diffusivity) must be used The results of one experiment to measure mass diffusivity have been published, but the grains size of the material used in this experiment was much smaller than is thought to apply to the landing site. However, when the grain size and shape are included in estimation of the pore size, the calculated Knudsen diffusivity is close to the experimental results. The effective mass diffusivity calculated for the landing site is three orders of magnitude larger than the experimental results, but consistent with different grain size and shape.

Physical properties of the regolith at the InSight landing site presented here are all speculative. Some of the properties are based on circular reasoning because they are based on data that were used to select the landing site, such as surface thermophysical properties. However, even these properties are ultimately based on correlations of remote sensing properties (satellite or rover) with ground truth data. Many of the properties are based on extensive experimental data with carefully refined models for the Mars regolith. However, with the exception of a shallow trench dug by the Phoenix lander in the southern polar region, and extrapolations from limited cliff exposures, there are no direct stratigraphic data describing the Mars regolith. We will gain much of these data during the penetration of the HP^3 probe and from the data collected during the InSight mission.

7. References

R. K. Agarwal, Y. Keon-Young, R. Balakrishnan, Phys. Fluids 13, 3061 (2001)

E. Albrecht, G. Baum, T. Bellunato, A. Bressan, S. Dalla Torre, C. D'Ambrosio, M. Davenport, M. Dragicevic, S. Duarte Pinto, P. Fauland, S. Ilie, G. Lenzen, P. Pagano, D. Piedigrossi, F. Tessarotto, and O. Ullaland, Nuclear Inst. and Methods in Res. A 510, 262 (2003)

K. A. Alshibli, A. Hasan, J. Geotech. Environ. Eng. 135, 673 (2009)

V. Ansan, V., T. Dezert (and the DLR group), InSight Science Team Presentation, Zurich, Switzerland, September 5–9, 2015, and written communication (2015)

R. E. Arvidson, P. Bellutta, F. Caley, A. A. Fraeman, J. B. Garvin, O. Gasnault, J. A. Grant, J. P. Grotzinger, V. E. Hamilton, M. Heverly, K. A. Lagnemma, J. R. Johnson, N. Lanza, S. Le Mouélic, N. Mangold, D. W. Ming, M. Hehta, R. V. Morris, H. E. Newsom, N. Rennó, D. Rubin, J. Schieber, R.

Sletten, N. T. Stein, F. Thuillier, A. R. Vasavada, J. Vizcaino, R. C. Wiens, J. Geophys. Res. Planets, 119, 1322 (2014) doi:10.1002/2013JE004605

D. Assimaki, W. Li, J. H. Steidl, K. Tsuda, Bull. Seism. Soc. Am. 98, 301 (2008) doi: 10.1785/0120070030

L. A. Aylmore, G., I. D. Sills, J. P. Quirk, Clay and Clay Minerals 18, 91 (1970)

R. Bachrach, J. Dvorkin, A. Nur, Geophysics 63, 1234 (1998)

R. Bachrach, J. Dvorkin, A. Nur, Geophysics 65, 559 (2000)

W. B. Banerdt, S. Smrekar, K. Hurst, P. Lognonné, T. Spohn, S. Asmar, D. Banfield, L. Boschi, U. Christensen, V. Dehant, W. Folkner, D. Giardini, W, Goetz, M. Golombek, M. Grott, T. Hudson, C. Johnson, G. Kargl, N. Kobayashi, J. Maki, D. Mimoun, A. Mocquet, P. Morgan, M. Panning, W. T. Pike, J. Tromp, T. vanZoest, R. Weber, M. Wiezorek, and the InSight Team, 44th Lunar and Planetary Science Conference (Lunar and Planetary Institute, Houston, Abstract #1915, 2013)

Becker A., C. Vrettos C., 5th ASCE International Conference on Engineering, Construction, and Operations in Challenging Environments. Earth and Space 2016, 9 (2016)

M. D. Bolton, Géotechnique 36, 65 (1986)

J. E.. Bowles, Foundation analysis and design (McGraw-Hill, New York, 1996)

Th. Brunet, X. Jia, P. Mills, Phys. Rev. Lett. 101, 138001 (2008) doi: 10.1103/PhysRevLett.101.138001

W. D. Carrier, Earth Moon Planets 10, 183 (1974) doi:10.1007/BF00655719.

W. D. Carrier, J. K. Mitchell, A. Mahmood, Proc. Lunar Sci. Conf., 4th, 4, 118 (Lunar and Planetary Institute, Houston, 1973)

D. C. Catling, C. B. Leovy, S. E. Wood, M. D. Day, 42nd Lunar and Planetary Science Conference (Lunar and Planetary Institute, Houston, Abstract #2529, 2011)

D. C. Catling, C. B. Leovy, S. E. Wood, M. D. Day, Third Conference on Early Mars (Lunar and Planetary Institute, Houston, Abstract #7031, 2012)

C. Charalambous, On the evolution of particle fragmentation with applications to planetary surfaces (Doctoral dissertation/thesis, Imperial College London, 2014/2015).

C. Charalambous, W.T. Pike, AGU Fall Meeting Abstracts, # P23B-3986 (2014)

C. Charalambous, W.T. Pike, W. Goetz, M.H. Hecht, U. Staufer, AGU Fall Meeting Abstracts, # P43B-1669 (2011)

P. R. Christensen, Icarus 68, 217 (1986)

P. R. Christensen, H.J. Moore, in MARS, ed. By H.H. Kieffer, B.M. Jakosky, C.W. Snyder, M.S. Matthews (University of Arizona Press, Tucson, 1992), p. 686

1404 P. R. Christensen, D.L. Anderson, S.C. Chase, R.N. Clark, H.H. Kieffer, M.C. Malin, J.C. Pearl, J. Carpenter,
1405 N. Bandiera, F.G. Brown, S. Silverman, J. Geophys. Res 97, 7719 (1992)
1406 P. R. Christensen, J.L. Bandfield, V.E. Hamilton, S.W. Ruff, H.H. Kieffer, T.N. Titus, M.C. Malin, R.V.
1407 Morris, M.D. Lane, R.L. Clark, B.M. Jakosky, M.T. Mellon, J.C. Pearl, B.J. Conrath, M.D. Smith, R.T.
1408 Clancy, R.O. Kuzmin, T. Roush, G.L. Mehall, N. Gorelick, K. Bender, S. Dason, E. Greene, S. Silverman,
1409 M. Greenfield, J. Geophys. Res. 106, 23823 (2001)
1410 P. R. Christensen, P. R., J. L. Bandfield, J. F. Bell III, N. Gorelick, V. E. Hamilton, A. Ivanov, B. M.
1411 Jakosky, H. H. Kieffer, M. D. Lane, M. C. Malin, T. McConnochie, A. S. McEwen, H. Y. McSween
1412 Jr., G. L. Mehall, J. E. Moersch, K. H. Nealson, J. W., Rice Jr., M. I. Richardson, S. W. Ruff, M. D.
1413 Smith, T. N. Titus, M. B. Wyatt, Science 300, 2056 (2003a)
1414 P. R. Christensen, G. L. Mehall, S. H. Silverman, S. Anwar, G. Cannon, N. Gorelick, R. Kheen, T.
1415 Tourville, D. Bates, S. Ferry, T. Fortuna, J. Jeffryes, W. O'Donnell, R. Peralta, T. Wolverton, D. Blaney,
1416 R. Denise, J. Rademacher, R. V. Morris, S. Squyres, J. Geophys. Res. 108 (2003b)
1417 doi:10.1029/2003JE002117
1418 P. R. Christensen, S. W. Ruff, R. L. Fergason, A. T. Knudson, S. Anwar, R. E. Arvidson, J. L. Bandfield,
1419 D. L. Blaney, C. Budney, W. M. Calvin, T. D. Glotch, M. P. Golombek, N. Gorelick, T. G. Graff, V.
1420 E. Hamilton, A. Hayes, J. R. Johnson, H. Y. McSween Jr., G. L. Mehall, L. K. Mehall, J. E. Moersch,
1421 R. V. Morris, A. D. Rogers, M. D. Smith, S. W. Squyres, M. J. Wolff, M. B. Wyall, Science 305, 837
1422 (2004a)
1423 P. R. Christensen, M. B. Wyatt, T. D. Glotch, A. D. Rogers, S. Anwar, R. E. Arvidson, J. L. Bandfield,
1424 D. L. Blaney, C. Budney, W. M. Calvin, A. Fallacaro, R. L. Fergason, N. Gorelick, T. G. Graff, V. E.
1425 Hamilton, A. G., Hayes, J. R. Johnson, A. T. Knudson, H. Y. McSween Jr., G. L. Mehall, L. K. Mehall,
1426 J. E. Moersch, R. V. Morris, M. D. Smith, S. W. Squyres, S. W. Ruff, M. J. Wolff, Science 306, 1733
1427 (2004b)
1428 P. R. Christensen, P. R., B.M. Jakosky, H.H. Kieffer, M.C. Malin, H.Y. McSween Jr., K. Nealson, G.L.
1429 Mehall, S.H. Silverman, S. Ferry, M. Caplinger, M. Ravine, Space Sci. Rev. 110, 85 (2004c)
1430 F. Civan, F., Trans. Porous. Media 82, 375 (2010)
1431 J. E. Conel, J. Geophys. Res. 74,1614 (1969)
1432 G. J. Consolmagno, M. W. Schaefer, B. E. Schaefer, D. T. Britt, R. J. Macke, M. C. Nolan, E. S. Howell,
1433 Planetary and Space Science 87, 146 (2013)
1434 M. R. Cooper, R.L. Kovach, J. S. Watkins, Rev. Geophys. Space Phys. 12, 291 (1974)
1435 A. M. Dainty, N. M. Toksöz, Phys. Earth Planet. Int. 26, 250 (1981)

1436 G. Dal Moro, Icarus 254, 338 (2015) doi:10.1016/j.icarus.2015.03.017
1437 I. J. Daubar, A. S. McEwen, M. P. Golombek, 46th Lunar and Planetary Science Conference (Lunar and
1438 Planetary Institute, Houston, Abstract #2225, 2015)
1439 P. Delage, F. Karakostas, A. Dhemaied, M. Belmokhtar, P. Lognonné, M. Golombek, E. De Laure, J.-C.
1440 Dupla, S. Kedar, Y.J. Cui, B. Banerdt, Space Sci. Rev. (2017) doi:10.1007/s11214-017-033907.
1441 S. A. Denekamp, Y. Tsur-Lavie, Journal of Geotechnical and Geoenvironmental Engineering 107, 439
1442 (1981)
1443 F. P. Fanale, W. A. Canon, J. Geophys. Res. 84, 8404 (1979)
1444 F. P. Fanale, W. B. Banerdt, R. S. Saunders, L. A Johansen, J. R. Salvail, J. Geophys. Res. 87, 10,215
1445 (1982a)
1446 F. P. Fanale. J. R. Savail, W. B. Banerdt, R. S. Saunders, Icarus 50, 381 (1982b)
1447 L. Y. Faust, Geophysics, 16, 192 (1951)
1448 W. C. Feldman, F. H. Prettyman, S. Maurice, J. J. Plaut, D. L. Bish, D. T. Vaniman, M. T. Mellon, A.
1449 E. Metzger, S. W. Squyres, S. Karunatillake, W. V. Bounton, R. C. Elphic, H. O. Funsten, D. J.
1450 Lawrence, R. L.Tokar, J. Geophys. Res. 109, E09006, (2004) doi:10.1029/2003JE002160
1451 R. L. Fergason, P. R. Christensen, H. H. Kieffer, J. Geophys. Res. 111, E12004 (2006a)
1452 doi:10.1029/2006JE002735
1453 R. L. Fergason, P. R. Christensen, J. F. Bell III, M. P. Golombek, K. E. Herkenhoff, H. H. Kieffer, J.
1454 Geophys. Res. 111, E02S21 (2006b) doi:10.1029/2005JE002583
1455 R. L. Fergason, P. R. Christensen, M .P. Golombek, T .J. Parker, Space Sci. Rev. 170, 739 (2012)
1456 doi:10.1007/s11214-012-9891-3
1457 C. N. Foley, T. Economou, R. N. Clayton, J. Geopys. Res. 108, 8096 (2003) doi:10.1029/2002JE002019
1458 V. Formisano, F. Angrilli, G. Arnold, S. Atreya, G. Bianchini, D. Biondi, A. Blanco, M. I. Blecka, A.
1459 Coradini, L. Colangeli, A. Ekonomov, F. Esposito, S. Fonti, M. Giuranna, D. Grassi, V. Gnedykh, A
1460 Grigoriev, G. Hansen, H. Hirsh, I. Khatuntsev, A. Kiselev, N. Ignatiev, A. Jurewicz, E. Lellouch, J.
1461 Lopez Moreno, A. Marten, A. Mattana, A. Maturilli, M. Michalska, V. Moroz, B. Moshkin, F. Nespoli,
1462 Y. Nikolsky, R. Orfei, P. Orleanski, V. Orleanski, V. Orofino, E. Palomba, D. Patsaev, G. Piccioni, M.
1463 Rataj, R. Rodrigo, J. Rodriguez, M. Rossi, B. Saggin, D. Titov, L. Zasova, Planet. Space Sci. 53, 963
1464 (2005) doi:10.1016/j.pss.2004.12.006
1465 J. Fortin, S. Stanchits, S. Vinciguerra, Y. Guéguen, Tectonophysics, 503, 60 (2011)
1466 doi:10.1016/j.tecto.2010.09.028
1467 J. A., Fountain, E. A. West, J. Geophys. Res. 75, 4063 (1970)

1468 N. Fujii, M. Osako, Earth Planet. Sci. Lett. 18, 65 (1973) doi:10.1016/0012-821X(73)90035-6
1469 R. Fukushima, H. Nakahara, T. Nishimura, Bull. Seismol. Soc. Am. 106, 552 (2016)
1470 doi:10.1785/0120150059
1471 A. F. Gangi, T. E. Yen, Moon and Planets, 20, 439 (1979)
1472 J. F. Gibbs, D. M. Boore, W. B. Joyner, T. E. Furnal, Bull. Seism. Soc. Am. 84, 76 (1994)
1473 K. L. Gillet, M. Margerin, M. Calvet, M. Monnereau, Phys. Earth. Planet. Int. 262, 28 (2017)
1474 doi:10.1016/j.pepi.2016.11.001
1475 M. P. Golombek and the Mars Pathfinder Science Team, J. Geophys. Res. 104, 8523 (1999)
1476 M. P. Golombek, R.J. Phillips, in Planetary Tectonics, ed. by T.R. Watters, R.A. Schultz (Cambridge
1477 University Press, Cambridge, Chap. 5, p. 183, 2010)
1478 M. P. Golombek, R.A. Cook, H.J. Moore, T.J. Parker, J. Geophys. Res. 102, 3967 (1997)
1479 M. P. Golombek, R. E. Arvidson, J. F. Bell III, P. R. Christensen, J. A. Crisp, L. S. Crumpler, B. L.
1480 Ehlmann, R. L. Fergason, J. A. Grant, R. Greeley, A. F. C. Haldermann, D. M. Kass, T. J. Parker, J.
1481 T. Schofield, S. W. Squyres, R. W. Zurek, Assessment of Mars Exploration Rover landing site
1482 predictions. Nature 436, 44 (2005) doi:10.1038/nature03600
1483 M. P. Golombek, L. S. Crumpler, J. A. Grant, R. Greeley, N. A. Cabrol, T. J. Parker, J. W. Rice Jr., J. G.
1484 Ward, R. E. Arvidson, J. E. Moersch, R. L. Fergason, P. R. Christensen, A. Castaño, R. Castaño, A.
1485 F. C. Haldermann, R. Li, J. F. Bell III, S. W. Squyres, J. Geophys. Res. 110, E02S07 (2006)
1486 doi:10.1029/2005JE002503
1487 M. P. Golombek, A. F. C. Haldemann, R. A. Simpson, R. L. Fergason, N. E. Putzig, R. E. Arvidson, J.
1488 F. Bell III, M. T. Mellon, in The Martian Surface: Composition, Mineralogy and Physical Properties, ed.
1489 by J. F. Bell III (Cambridge University Press, Cambridge, Chap. 21, pp. 468, 2008a)
1490 M. P. Golombek, A Huertas, J. Marlow, B. McGrane, C Klein, M Martinez, R. E. Arvidson, T. Heet, L.
1491 Barry, K. Seelos, D. Adams, W. Li, J. R. Matijevic, T. Parker, H. G. Sizemore, M. Mellon, A. S.
1492 McEwen, L. K. Tamppari, Y. Cheng, J. Geophys. Res. 113, E00A09 (2008b) doi:10.1029/2007JE003065
1493 M. P. Golombek, A. Huertas, D. Kipp, F. Calef, Mars 7, 1 (2012) doi:10.1555/mars.2012.0001
1494 M. P. Golombek, N. Warner, C. Schwartz, J. Green, 2013, 44th Lunar and Planetary Science Conference
1495 (Lunar and Planetary Institute, Houston, Abstract #1696, 2013b)
1496 M. P. Golombek, D. Kipp, N. Warner, I. J. Daubar, R. Ferguson, R. Kirk, R. Beyer, A. Huertas, S. Piqueux,
1497 N. Putzig, B. A. Campbell, G. A. Morgan, C. Charalambous, T. Pike, K. Gwinner, F. Calef, J. Ashley,
1498 D. Kass, M. Mischna, C. Bloom, N. Wigton, C. Schwartz, H. Gengl, L. Remond, J. Sweeney, E.

Sklyanskiy, M. Lisano, J. Benardino, S. Smrekar, and B. Banerdt, Space Sci. Rev. 211, 5 (2017) doi:10.1007/s11214-016-0321-9.

J. Gomez-Elvira, C. Armiens, L. Castañer, M. Domínguez, M. Genzer, F. Gómez, R. Haberle, A.-M. Harri, V. Jiménez, H. Kahanpää, L. Kowalski, A. Lepinette, J. Martin, J. Martínez-Frías, I McEwan, L. Mora, J. Moreno, S. Navarro, M. A. de Pablo, A. Peña, J. Polkko, M. Ramos, N. O. Renno, J. Ricart, M. Richardson, J. Rodríguez-Manfredi, J. Romeral, E. Sebastián, J. Serrano, M. de la Torre Juárez, J. Torrez, F. Torrero, R. Urquí, L. Vázquez, T. Velasco, J. Verdasca, M.-P. Zorzano, J. Martin-Torres, Space Sci. Rev 170, 583 (2012)

S. Griffiths, A. Rescaglio, C. Krause, Ultrasonics, 50, 139 (2010) doi:10.1016/j.ultra.2009.09.034

M. Grott, J. Helbert, R. Nadalini J. Geophys. Res., 112, E09004 (2007) doi:10.1029/2007JE002905.

B. Gundlach, J. Blum, Icarus 223, 479 (2013)

V. E. Hamilton, A. R. Vasavada, E. Sebastían, M. de la Torre Juárez, M. Ramos, C. Armiens, R. E. Arvidson, I. Carrasco, P. R. Christensen, M. A. de Pablo, W. Goetz, J. Gómez-Elvira, M. T. Lemmon, M. B. Madsen, F. Javier Martin-Torres, J. Martínez-Frías, A. Molina, M. C. Palucis, S. C. R. Rafkin, M. I. Richardson, R. A. Yingst, M.-P. Zorzano, J. Geophys. Res. 119, 745 (2014) doi:10.1002/2013JE004520.

W. K. Hartmann, J. Anguita, M. de la Casa, D. Berman, E.V. Ryan, Icarus 149, 37 (2001)

L. A. Haskin, A. Wang, B. L. Jolliff, H. Y. McSween, B. C. Clark, D. J. Des Marais, S. M. McLennan, N. J. Tosca, J. A. Hurowitz, J. D. Farmer, A. Yen, S. W. Squyres, R. E. Arvidson, G. Klingelhöfer, C. Schröder, P. A. De Souza Jr., D. W. Ming, R. Gellert, J. Zipfel, J. Brückner, J. F. Bell III, K Herkenhoff, P. R. Christensen, S. Ruff, D. Blaney, S. Gorevan, N. A. Cabrol, L. Crumpler, J. Grant, L. Soderblom, Nature 436, 66 (2005).

G. Heiken, D. Vaniman, B. French, eds., Lunar Sourcebook (Cambridge Univ. Press, Cambridge, U. K., 1991)

B. S. Hemingway, R. A. Robie, W. H. Wilson, Proceedings of the Lunar Science Conference 4, 2481 (1973)

K. E. Herkenhoff, M. P. Golombek, E. A. Guinness, J. B. Johnson, A. Kusack, L. Richter, R. J. Sullivan, S. Gorevan, in: J.Bell, ed.,The Martian Surface (Cambridge University Press, Cambridge, UK, 2008)

H. Hertz, Gesammelte Werke (v. 1, p. 155, Leipzig, 1895)

S. L. Hess, R. M. Henry, J. E, Tillman (1979), J. Geophys. Res. 84, 2923 (1979) doi:10.1029/JB084iB06p02923.

P. G., Horvath, V. Latham, Y. Nakamura, H. J. Dorman, J. Geophys. Res., 85, 6572 (1979)

D. G. Huizenga, D. M. Smith, Am. Inst. Chem. Eng (AIChE) J. 32, 1 (1986)

J. A. Hurowitz, S. M. McLennan, N. J. Tosca, R. E. Arvidson, J. R. Michalski, D. W. Ming, C. Schröder, S. W. Squyres, J. Geophys. Res. 111, E02S19 (2006).

E. S. Hütter, N. I. Koemle, G. Kargl, E. Kaufmann, J. Geophys. Res, 113, E12004 (2008) doi:10.1029/2008JE003085

M. B. Jaksa, K. S. Yeong, K. T. Wong, S. L. Lee, Proc. 9th Australia New Zealand Conference on Geomechanics (Auckland, New Zealand, p. 289-294, 2004)

J. Jaky, J. Soc. Hung. Eng. Arch. (Magyar Mernok es Epitesz-Egylet Kozlonye, in Hungarian, p. 355 1944)

F. Javadpour, D. Fisher, M. Unsworth, J. Canadian Petrol. Tech. 46 55 (2007)

D. M. Johnson, A. L. Frisillo, J. Dorman, G. V. Latham, D. Strangway, J. Geophys. Res. 87, 1899 (1982)

B. W. Jones, Proceedings Third Lunar Sci. Conf. p. 2545 (1972)

D. Jongmans, Eng. Geology 29, 99 (1990)

M. G. Kaganer, J. Eng. Phys. 11, 19 (1966)

G. Karnaidakis, A. Beskok, N. Aluru, 2005, Microflows and Nanoflows: Fundamentals and Simulation, (Springer, New York. 2005)

M. Kaviany, Principles of Convective Heat transfer (Springer, 2nd edn. 2001)

S. J. Keihm , K Peters, M. G. Langseth Jr., J. L. Chute Jr., Earth Planet. Sci. Lett. 19, 337 (1973)

S. J. Keihm and Langseth Jr., Proceed. 4th Lunar Sci. Conf. 3, 2503 (1973)

S. J. Keihm, M. G. Langseth Jr., Icarus 24, 211 (1975

H. H. Kieffer, J. Geophys.Res. Planets 118, 451 (2013)

H. H. Kieffer, T. Z. Martin, A. R. Peterfreund, B. M. Jakosky, E. D. Miner, F. D. Palluconi, J. Geophys. Res. 82, 4249 (1977)

S. Kinoshita, Bull. Seism. Soc. Am. 98, 463 (2008) doi:10.1785/0120070070

L. J. Klinkenberg, API Drilling and Production Practices (New York, p. 200, 1941)

B. Knapmeyer-Endrun, M.P. Golombek, M. Ohrnberger, Space Sci Rev., doi: 10.1007/s11214-016-0300-1

J. F. Kok, E. J. Parteli, T. I. Michaels, D. B. Karam, 2012, Reports on Progress in Physics, 106901 (2012)

R. L. Kovach, J. S. Watkins, Lunar Planet. Sci. Conf. 3, 461 (1972)

R. L. Kovach, J.S. Watkins, Moon, 7, 63 (1973)

M. G. Langseth Jr, S. J. Keihm, K. Peters, Proc. 7th Lunar Sci. Conf. (Lunar and Planet. Inst. Houston, p. 3143, 1976)

E. Larose, A. Khan, Y. Nakamura, M. Campillo, Geophys. Res. Lett., 32, L16201 (2005) doi:10.1029/2005GL023518

G. V. Latham, M. Ewing, F. Press, G. Sutton, J. Dorman, Y. Nakamura, N. Toksöz, R. Wiggins, J. Derr, F. Duennebier, Passive seismic experiment. Science 167, 445 (1970a)

G. V. Latham, M. Ewing, J. Dorman, F. Press, N. Toksöz, G. Sutton, R. Meissner, F. Duennebier, Y Nakamura, R. Kovach, M. Yates, 170, 620 (1970b)

T. Lay, T. C. Wallace, in Moden Global Seismology (Academic Press, San Diego, p.104, 1995)

K. Lee, H. Seed, J. Soil Mech. Foundation Divn. ASCE 93, 117 (1967)

R. B. Leighton, B.C. Murray, Science, 153, 136 (1966)

L. A. Leshin, P. R. Mahaffy, C. R. Webster, M. Cabane, P. Coll, P. G. Conrad, P. D. Archer Jr., S. K. Atreya, A. E. Brunner, A. Buch, J. L. Eigenbrode, G. J. Flesch, H. B. Franz, C. Freissinet, D. P. Glavin, A. C. McAdam, K. E. Miller, D. W. Ming, R. V. Morris,R. Navarro-González, P. B. Niles, T. Owen, R. O. Pepin, S. Squyres, A. Steele,J. C. Stern, R. E. Summons, D. Y. Sumner, B. Sutter, C. Szopa, S. Teinturier, M. G. Trainer, J. J. Wray, J. P. Grotzinger and MSL Science Team, Science, 341, (2013) doi:10.1126/science.1238937

Y. Liang, J. D. Price, D. A. Ward, E. B. Watson, J. Geophys. Res. 106, 529 (2001)

R. Lichtenheldt, Lokomotorische Interaktion planetarer Explorationssysteme mit weichen Sandböden (Verlag Dr. Hut, ISBN 978-3-8439-2704-8, Munich, 2016)

P. Lognonné, B. Mosser, Surv. Geophys. 14, 239 (1993)

P. Lognonné, M. Le Feuvre, C. L. Johnson, R. C. Weber, J. Geophys. Res, 114, E12003 (2009) doi:.1029/2008JE003294

A. Lorek, N. Wagner, Cryosphere, 7, 1839 (2013) doi:10.5194/tc-7-1839-2013

L. Malagnini, Bull. Seism. Soc. Am., 86, 1471 (1996)

L. Malagnini, R. B. Herrmann, G. Biella, R. de Franco, Bull. Seism. Soc. Am., 85, 900 (1995)

N. Mark, G. H. Sutton, J. Geophys. Res., 80, 4932 (1975)

F. J. Martın-Torres, M.-P. Zorzano, P. Valentin-Serrano, A.-M. Harri, M. Genzer, O. Kemooinen, E. G. Rivera-Valentin, I. Jun, J. Wray, M. B. Madsen, W. Goetz, A. S. McEwen, C. Hardgrove, N. Renno, V. F. Chevrier, M. Mischna, R. Navarro-González, J. Martinez-Frías, P. Conrad, T. McConnochie, C. Cockell, G. Berger, A. R. Vasavada, D. Sumner, David. Vaniman, Nature Geosci. 8, 357 (2015) doi:10.1038/ngeo2412

1592 G. M. Martinez, N. Rennó, E. Fischer, C. S. Borlina, B. Hallet, M. De la Torre Juárez, A. R. Vasavada, M.
1593 Ramos, V. Hamilton, J. Gomez-Elvira, R. M. Haberle, J Geophys Res Planets 119, 1822, (2014)
1594 doi:10.1002/2014JE004618
1595 G. M. Martinez, A. De-Vicente-Retortillo, A. G. Fairén, E. Fischer, S. D. Guzewich, R, M, Haberle, H.
1596 Kahanpää, O. Kemppinen, M. Lemmon, C. Newman, N. Renno, M. Richardson, M. D. Smith, M. Torre-
1597 Juárez, A. Vasavada, Space Sci Rev 212, 295 (2017) doi:10.1007/s11214-017-0360-x
1598 W. J. Massmann, J. Geophys. Res. 111, (2006) doi:10.1029/2006JG000163.
1599 J. Massmann, D. F. Farrier, Water Resources Res., 28, 777 (1992)
1600 I. O. McGlynn, C. M. Fedo, H. Y. McSween Jr., J. Geophys. Res., 116, E00F22, (2011)
1601 doi:10.1029/2010JE003712.
1602 D. S. McKay J. L. Carter W. W. Boles C. Allen C., J. Allton J., Engineering, Construction, and Operations
1603 in Space IV American Society of Civil Engineers, p. 857 (1994)
1604 M. Mehta, N. O. Renno, J. Marshall, M. R. Grover, A. Sengupta, N. A. Rusche, J. F. Kok, R. E. Arvidson,
1605 W. J. Markiewicz, M. T. Lemmon, P. H. Smith, Icarus 211, 172 (2011)
1606 doi:10.1016/j.icarus.2010.10.003
1607 M. Mehta, A. Sengupta, N. O. Rennó, J. W. Norman, P. G. Van, Huseman, D. S. Gulick, M. Pokora,
1608 M., AIAA J. 51, 2800 (2013) doi:10.2514/1.J052408
1609 H. J. Melosh, H. J., Impact Craters, A Geologic Process (Oxford University Press, London, 1989)
1610 M. T. Mellon, B.M. Jakosky, H.H. Kieffer, P.R. Christensen, Icarus 148, 437–455 (2000)
1611 M. T. Mellon, R. L. Fergason, N. E. Putzig, in The Martian Surface: Composition, Mineralogy and Physical
1612 Properties, ed. by J.F. Bell III (Cambridge University Press, Cambridge, Chap. 19, p. 399, 2008)
1613 P.-Y. Meslin, O. Gasnault, O. Forni, S. Schröder, A. Cousin, G. Berger, S. M. Clegg, J. Lasue, S. Maurice,
1614 V. Sautter, S. Le Mouélic, R. C. Wiens, C. Fabre, W. Goetz, D. Bish, N. Mangold, B. Ehlmann, N.
1615 Lanza, A.-M. Harri, R. Anderson, E. Rampe, T. H. McConnochie, P. Pinet, D. Blaney, R. Léveillé, D.
1616 Archer, B. Barraclough, S. Bender, D. Blake, J. G. Blank, N. Bridges, B. C. Clark, L. DeFlores, D.
1617 Delapp,G. Dromart, M. D. Dyar, M. Fisk, B. Gondet, J. Grotzinger, K. Herkenhoff, J. Johnson, J.-L.
1618 Lacour, Y. Langevin, L. Leshin, E. Lewin, M. B. Madsen, N. Melikechi, A. Mezzacappa, M. A. Mischna,
1619 J. E. Moores, H. Newsom, A. Ollila, R. Perez, N. Renno, J.-B. Sirven, R. Tokar, M. de la Torre, L.
1620 d'Uston, D. Vaniman, A. Yingst and MSL Science Team, Science, 341 (2013)
1621 doi:10.1125/science.128670
1622 R. E. Milliken, J.F. Mustard, F. Poulet, D. Jouglet, J.-P. Bibring, B. Gondet and Y. Langevin, J. Geophys.
1623 Res., 112, E08S07 (2007) doi:10.1029/2006JE002853

1624 D. Mimoun, D. Murdoch, P. Lognonné, K. Hurst, W. T. Pike, J. Hurley, T. Nébut, W. B. Banerdt and
1625 the SEIS Team, Space Sci. Rev. 211, 383 (2017) doi:10.1007/s11214-017-0409-x
1626 D. T. F. Möhlmann, Icarus 168, 318 (2004) doi:10.1016/j.icarus.2003.11.008
1627 D. T. F. Möhlmann, Icarus 195, 131 (2008) doi:10.1016/j.icarus.2007.11.026
1628 H. J. Moore, B.M. Jakosky, Icarus 81, 164 (1989)
1629 H. J. Moore, R. E. Hutton, G. D. Clow, C. R. Spitzer, USGS Prof. Paper 1389, 222pp., 2 plates (1987)
1630 H. J. Moore, R. E. Hutton, R. F. Scott, C. R. Spitzer, R. W. Shorthill, J. Geophys. Res. 82, 4497 (1977)
1631 H. J. Moore, D. B. Bickler, J. A. Crisp, H. J. Eisen, J. A. Gensler, A. F. C. Haldemann, J. R. Matijevic,
1632 L. K. Reid, F. Pavlics, J. Geophys. Res. 104, 8729 (1999)
1633 P. Morgan, S. E. Smrekar, R. Lorenz, M. Grott, O. Kroemer, N. Müller, Space Sci. Rev. 211, 277 (2017)
1634 doi:10.1007/s11214-017-0388-y
1635 K. Mueller, M. P. Golombek, Ann. Rev. Earth Planet. Sci. 32, 435 (2004)
1636 N. Murdoch, B. Kenda, T. Kawamura, A. Spiga, P. Lognonné, D. Mimoun, W. B. Banerdt, Space Sci.
1637 Rev. 211, 457 (2017a) doi:10.1007/s11214-017-0343-y
1638 N. Murdoch, D Mimoun, R. F. Garcia, W. Rapin, T. Kawamura, P. Lognonné, D. Banfield, W. B. Banfield,
1639 Space Sci. Rev. 211,429 (2017b) doi:10.1007/s11214-016-0311-y
1640 Y. Nakamura, J. Dorman, F. Duennebier, D. Lammlein, G. Latham, The Moon, 13, 57 (1975)
1641 Y. Nakamura, Bull. Seism. Soc. Am., 66, 593 (1976)
1642 Y. Nakamura, J. Koyama, J. Geophys. Res., 87, 4855 (1982)
1643 Y. Nakamura, F. Duennebier, G. Latham, F. Dorman, J. Geophys. Res. 81, 4818 (1976)
1644 R. Nave, 2016, Mean Free Path, Hyperphysics (website hosted by Dept. Physics and Astronomy, Georgia
1645 State Univ. 2016, http://hyperphysics.phy-astr.gsu.edu/hbase/Kinetic/menfre.html. (last accessed
1646 2017-3-13).
1647 G. Neugebauer, G. Münch, H. Kieffer, S. C. Chase Jr, E. Miner, Astron. J. 76, 719 (1969)
1648 R. H. Nilson, E. W. Peterson, K. H. Lie, N. R., Burkhard, J. R. Hearst, J. Geophys. Res., 96, 21,933 (1991)
1649 S. A. Nowicki, P.R. Christensen, J. Geophys. Res. 112, E05007 (2007). doi:10.1029/2006JE002798
1650 Y. Ohsaki, R. Iwasaki, Soils and Foundations, 13, 61 (1973)
1651 F. D. Palluconi, H.H. Kieffer, Icarus 45, 415 (1981)
1652 B. I. Pandit, D. C. Tozer, Nature, 226, 335 (1970)
1653 S. Parolai, D. Bindi, A. Ansal, A. Kurtulus, A. Strollo, J. Zschau, Geophys. J. Int. 181, 1147 (2010)
1654 doi:10.1111/j.1365-246X.2010.04567.

1655 M. D. Paton, A.-M Harri, H. Savijärvi, T. Mäkinen, A. Hagermann, O. Kemppinen, A. Johnston, Icarus
1656 271, 360 (2016)
1657 W. T. Pike, U. Staufer, M. H. Hecht, W. Goetz, D. Parrat, H. Sykulska-Lawrence, S. Vijendran, M. B.
1658 Madsen, Geophysical Research Letters, 38, L24201 (2011) doi:10.1029/2011GL049896
1659 C. C. Pilbeam, J. R. Vaišnys, J. Geophys. Res. 78, 810 (1973)
1660 S. Piqueux, P. R. Christensen, J. Geophys. Res. 114, E09005 (2009a) doi:10.1029/2008je003308.
1661 S. Piqueux, P. R. Christensen, J. Geophys. Res. 114, E09006 (2009b). doi:10.1029/2008je003309
1662 S. Piqueux, P. R. Christensen, J. Geophys. Res. 116, E07004 (2011) doi: 10.1029/2011je003805.
1663 S. Planke, E. Alvestad, O. Eldholm, The Leading Edge, 18, 342 (1999)
1664 A.-C. Plesa, M. Grott, M. T. Lemmon, N. Müller, N. Piqueux, M. A. Siegler, S. E. Smrekar, T. Spohn, J.
1665 Geophys. Res. Planet. 121, 2166 (2016) doi:10.1002/2016JE005127.
1666 L. K. Pleskot, E.D. Miner, Icarus 45, 179 (1981) Smith
1667 M. Prasad, R. Meissner, Geophysics, 57, 710 (1992)
1668 M. Prasad, M.A. Zimmer, P.A. Berge, B.P. Bonner, Tech. Rep. UCRL-JRNL-205155 (Lawrence Livermore
1669 National Laboratory, USA, 2004)
1670 M. A. Presley, P. R. Christensen (1997a), J. Geophys. Res. 102, 9221 (1997a) doi:10.1029/97JE00271.
1671 M. A. Presley, P. R. Christensen (1997b), J. Geophys. Res. 102, 6551 (1997b)
1672 N. E. Putzig, PhD Thesis (University of Colorado, Boulder, 2006)
1673 N. E. Putzig, M.T. Mellon, Icarus 191, 68 (2007) doi:10.1016/j.icarus.2007.1005.1013
1674 N. E Putzig, N. E. Mellon, R.E. Arvidson, K.A. Kretke, 2005, Icarus 173, 325 (2005)
1675 A. Revil, D. Grauls, O. Brévart, J. Geophys. Res., 107, 2293, (2002) doi:10.1029/2001JB000318, 2002.
1676 R. A. Robie, B. S. Hemingway, W. H. Wilson, Science, 167, 749 (1970)
1677 doi:10.1126/science.167.3918.749.
1678 A. Robinson, J. Gluyas, Marine and Petroleum Geology 9, 319 (1992)
1679 J. Rossabi, in C. Ho, S. Webb, eds., Gas Transport in Porous Media (Springer, Ch. 16, 279, 2006)
1680 J. Rossabi, R. W. Falta, Ground Water, 40, 67 (2002)
1681 S. Roy, R. Raju, H. F. Chuang, B. A. Cruden, M. Meyyappan, J. Appl. Phys. 93, 4870 (2003)
1682 S. W. Ruff, P.R. Christensen, 2002, J. Geophys. Res. 107, 5127 (2002) doi:10.1029/2001JE001580
1683 S. W. Ruff, P. R. Christensen, D. L. Blaney, W. H. Farrand, J. R. Johnson, J. R. Michalski, J. E. Moersch,
1684 S. P. Wright, S. W. Squyres, J. Geophys. Res., 111, E12S18 (2006) doi:10.1029/2006JE002747
1685 N. Sakatani, K. Ogawa Y. Iijima M. Arakawa S. Tanaka S., 2016, Icarus 267, 1 (2016)
1686 doi.org/10.1016/j.icarus.2015.12.012

1687 J. C. Santamarina, K. A. Klein, M. A. Fam, Soils and waves (Wiley, New-York, 2001)
1688 B. R. Scanlon, J. P. Nicot, J. W. Massmann, in Soil Physics Companion, A. W. Warrick, ed. (CRC Press,
1689 Chap. 8, p. 297 2002) doi: 10.1201/9781420041651.
1690 E. Schreiber, Proc. 8th Lun. Sci. Conf. 1201 (1977)
1691 R. F. Scott, Géotechnique, 37, 423 (1987)
1692 C. Sens-Schönfelder, E. Larose, Earthqake Sci. 23, 519 (2010) doi:10.1007/s11589-010-0750-6
1693 A. Shaw, R. E. Arvidson, R. Bonitz, J. Carsten, H. U. Keller, M. T. Lemmon, M. T. Mellon, M. Robinson,
1694 A. Trebi-Ollennu, J. Geophys. Res., 114, E00E05 (2009) doi:10.1029/2009JE003455.
1695 E. M. Shoemaker, E.C. Morris, Thickness of the regolith, in Surveyor: Program Results, (NASA Special
1696 Paper, v. 184 p. 96, U.S. Government Printing Office, Washington, 1969)
1697 D. E. Smith, M. T. Zuber, H. Frey J. B. Garvin. J. W. Head, D. O. Muhleman, G. H. Pettengill, R. J.
1698 Phillips, S. C. Solomon, H. J. Zwally, W. B. Banerdt, T. C. Duxbury, M. P. Golombek, F. G. Lemoine,
1699 G. A. Neumann, D. D. Rowlands, O. Aharonson, P. G. Ford, A. B. Ivanov, C. L. Johnson, P. J.
1700 McGovern, J. B. Abshire, R. S. Afzal, X. Sun, J. Geophys. Res. 106, 23,689 (2001)
1701 P. H. Smith, L. Tamppari, R. E. Arvidson, D. Bass, D. Blaney, W. Boynton, A. Carswell, D. Catling, B.
1702 Clark, T. Duck, T. Duck, E. Dejong, D. Fisher, W. Goetz, P. Gunnlaugsson, M. Hecht, V. Hipkin, J.
1703 Hoffman, S. Hviid, H. Keller, S. Kounaves, C. F. Lange, M. Lemmon, M. Madsen, M. Malin, W.
1704 Markiewicz, J. Marshall, C. McKay, M. Mellon, D. Michelangeli, D. Ming, R. Morris, N. Renno, W. T.
1705 Pike, U. Staufer, C. Stoker, P. Taylor, J. Whiteway, S. Young, A. Zent, J. Geophys, Res., 113, E00A18
1706 (2009) DOI:10.1029/2008JE003083, 16 pp.
1707 S. W. Squyres, R. E. Arvidson, J. F. Bell III, J. Brückner, N. A. Cabrol, W. Calvin, M. H. Carr, P. R.
1708 Chtritensen, B. C. Clark, L. Crumpler, D. J. Des Marais, C. d'Uston, T. Economou, J. Farmer, F.
1709 Farrand, W. Folkner, M. Golombek, S. Gorevan, J. A. Grant, R. Greeley, J. Grotzonger, L. Haskin, K.
1710 E. Herkenhoff, S. Hviid, J. Johnson, G. Klingelhöfer, A. Knoll, G. Landis, M. Lemmon, R. Li, M. B.
1711 madsen, M. C. Malin, S. M. McLennan, H. Y. McSween, D. W. ming, J. Moersch, R. V. Morris, T.
1712 Parker, J. W. Rice Jr, L. Richter, R. Rieder, M. Sims, M. Smith, P. Smith, L. A. Soderblom, R. Sullivan,
1713 H. Wänke, T. Wdowiak, M. Wolff, A. Yen, 2004, Science 305, 794 (2004) doi:10.1126/science.1100194
1714 L. Soderblom, R. C. Anderson, R. E. Arvidson, J. F. Bell III, N. A. Cabrol, W. Calvin, P. R. Christensen,
1715 B. C. Clark, T. Economou, B. L. Ehlmann, W. H. Farrand, D. Fike, R. Gellert, T. D. Glotch, M. P.
1716 Golombek, R. Greeley, J. P. Grotzonger, K. E. Herkenhoff, D. J. jerolmack, J. R. Johnson, B. Jolliff,
1717 G. Klingelhöfer, A. H. Knoll, Z. A. Learner, R. Li, M. C. Malin, S. M. McLennan, H. Y. McSween, D.

W. Ming, R. V. Morris, J. W. Rice Jr, L. Richter, R. Rieder, D. Rodionov, C. Schröder, F. P. Seelos IV, J. M. Soderblom, S. W. Squyres, R. Sullivan, W. A. Watters, C. M. Weitz, M. B. Wyatt, A. Yen, J. Zipfel, Science 306, 1723 (2004)

D. Sollberger, C. Schmelzbach, J. O. A. Robertsson, S. A. Greenhalgh, Y. Nakamura, A. Khan, Geophys. Res. Lett., 43 (2016) doi:10.1002/2016GL070883

S. Stanchits, S. Vinciguerra, G. Dresen, Pure Appl. Geophys. 163, 974 (2006) doi:10.1007/s00024-006-0059-5

R. Sullivan, R. Anderson, J. Biesiadecki, T. Bond, H. Stewart, J. Geophys. Res., 116, E02006 (2011) doi:10.1029/2010JE003625.

G. H. Sutton, F. K. Duennebier, J. Geophys. Res., 75, 7439 (1970)

Z. Tan, 2014, Basic properties of gases, in Air Pollution and Greenhouse Gases, From Basic Concepts to Engineering Applications for Air Emission Control (Springer, Singapore, p. 27, 2014) http://www.springer.com/cda/content/document/cda_downloaddocument/9789812872111-c2.pdf?SGWID=0-0-45-1486659-p176923844 (pdf download; last accesses 2017-3-15).

T. Tanaka, J. A. Skinner, J. M. Dohm, R. P. Irwin III, E. J. Kolb, C. M. Fortezzo, T. Platz,G. G. Michael, T. M. Hare, Geologic Map of Mars. (U.S. Geol. Surv. Sci. Invest. Map 3292, 2014)

T. Tanimoto, M. Eitzel, T. Yano, J. Geophys. Res. 113, E08011 (2008) doi:10.1029/2007JE003016

N. Teanby, J. Stevanović, J. Wookey, N. Murdoch, J. Hurley, R. Myhill, N. E. Bowles, S. B. Calcutt, W. T. Pike, Space Sci. Rev. ??, ??? (2016) doi:10.1007/s11214-016-0310-z

B. R. Tittmann, Phil. Trans. R. Soc. Lond. A, 285, 475 (1977)

B. R. Tittmann, M. Abdel-Gawad, R. M. Housley, in Proc. 3rd Lunar Sci. Conf. p. 2565 (1972)

B. R. Tittmann, H. Nadler, V. Clark, L. Coombe, in Proc. 10th Lunar Planet. Sci. Conf. p. 2131 (1979)

B. R. Tittmann, V. A. Clark, J. M. Richardson, T. W. Spencer, J. Geophys. Res. 85, 5199 (1980)

N. M. Toksöz, D. H. Johnson, A. Timur, Geophysics, 44, 681 (1979)

N. J. Tosca, S. M. McLennan, D. H. Lindsley, M. A. A. Schoonen, J. Geophys. Res., 109, E05003 (2004) doi:10.1029/2003JE002218.

O. Uyanik, (2010) Int. J. Phys. Sci., 5, 1034 (2010)

A. R. Vasavada, D. A. Paige, S. E. Wood, Icarus, 141, 179 (1999) doi:110.1006/icar.1999.6175.

A. R. Vasavada, S. Piqueux, K. W. Lewis, M. T. Lemmon, M. D. Smith, Icarus 284, 372 (2017)

D. Velea, F. D. Shields, J. M. Sabatier, Soil Sci. Soc. Am. J., 64, 1226 (2000)

V. Vesovic, W. A. Wakeham, G. A. Olchowy, J. V. Sengers, J. T. R. Watson, J. Millar, J. Phys. Chem. Ref. Data, 19, 763 (1990)

S. Vinciguerra, C. Trovato, P.G. Meredith, P.M. Benson, Int. J. Rock Mech. Min. Sci., 42, 900 (2005) doi:10.1016/j.ijrmms.2005.05.022

C. Vrettos, A. Becker, K. Merz, L. Witte, Earth and Space 2014, 14th ASCE International Conference on Engineering, Science, Construction and Operations in Challenging Environments (2014)

N. H. Warner, M.P. Golombek, C. Bloom, N. Wigton, C. Schwartz, 45th Lunar Planetary Science Conference (Lunar and Planetary Institute, Houston, Abstract #2217, 2014)

N. H. Warner, M.P. Golombek, J. Sweeney, A. Pivarunas, 47th Lunar Planetary Science Conference (Lunar and Planetary Institute, Houston, Abstract #2231, 2016)

N. H. Warner, M. P. Golombek, J. Sweeney, R. Fergason, R. Kirk, C. Schwartz, Space Sci. Rev. 211, 147 (2017) doi:10.1007/s11214-017-0352-x

J. S. Watkins, R. Kovach, Science 175, 1244 (1972)

J. S. Watkins, R. Kovach, Geochim. Cosmochim. Acta (Suppl.) 3, 2561 (1973)

J. S. Watkins, L. A. Walters, R. H. Godson, Geophysics 37, 29 (1972)

S. Whitaker, Transp. Porous Med. 25, 27 (1996)

B. B. Wilcox, M.S. Robinson, P.C. Thomas, B.R. Hawkes, Meteor. Planet. Sci. 40, 695 (2005)

D. F. Winter, J. M. Saari, Astrophys. J. 156, 1135 (1969) doi:10.1086/150041.

A. Yen, R. Gellert, C. Schröder, R. V. Morris, J. F. Bell III, A. T. Knudson, B. C. Clark, D. W. Ming, J. A. Crisp, R. E. Arvidson, D. Blaney, J. Brückner, P. R. Christensen, D. J. DesMarais, P. A. de Souza Jr, T. E. Economou, A. Ghosh, B. C. Hahn, K. E. Herkenhoff, L. A. Haskin, J. A. Hurowitz, B. L. Joliff, J. R. Johnson, G. Klingelhöfer, M. B. Madsen, S. M. McLennan, H. Y. McSween, L. Richter, R. Rieder, D. Rodionov, L. Soderblom, S. W. Squyres, N. J. Tosca, A. Wang, M. Wyatt, J. Zipfel, (2005). Nature, 436, 49 (2005) doi:10.1038/nature03637

K. Yomogida, T. Matsui, J. Geophys. Res. 88, 9513 (1983)

A. S. Ziarani, R. Aguilera, 2012, Transp. Porous Med., 91, 239 (2012) doi:10.1007/s11242-011-9842-6.

M. A. Zimmer, M. Prasad, G. Mavko, The Leading Edge 21, 178 (2002) doi:10.1190/1.1452609

M. A. Zimmer, M. Prasad, G. Mavko, A. Nur, Geophysics, 72, E1 (2007) doi:10.1190/1.2399459

8. Appendix

Soil mechanical parameters, definitions, and units. Units indicated by empty brackets are dimensionless.

Parameter	Notation - definition	Unit
Volume of the voids	V_v	m^3
Volume of the solid grains	V_s	m^3
Volume of the soil	$V = V_v + V_s$	m^3
Mass of the solid grains	M_s	kg
Mass of the soil	M ($M = M_s$ in dry soils)	kg
Specific gravity of the grains	ρ_s	kg/m^3
Bulk density oft he soil	ρ	kg/m^3
Void ratio (pores between the grains)	$e = V_v / V_s = n / (1 - n)$	[ ]
Porosity	$n = V_v / (V_v + V_s) = e / (1 + e) = 1 - (\rho_b / \rho_s)$	[ ]
Unit mass of the soil (bulk density)	$\rho = M / V = \rho_s(1 - n)$	kg/m^3
Maximum void ratio (minimum bulk	e_{max}	[ ]
Minimum void ratio (maximum bulk	e_{min}	[ ]
Relative density (or density index)	$D_r = (e_{max} - e)/(e_{max} - e_{min})$	%
D_{60} (from grain size distribution curve)	60% of the grains have diameter smaller than	µm
D_{10} (from grain size distribution curve)	10% of the grains have diameter smaller than	µm
Angle of internal friction	ϕ Shear strength parameter	°
Strain	ε	[ ]
Youngs modulus	E	[ ]
Poissons ratio	ν	[ ]
Compressional wave velocity	v_p	m/s
Shear wave velocity	v_s	m/s
Seismic quality factor	Q	[ ]